Development of a Sensor for Inflight Detection of Three-Dimensional Flow Separation on a Wing

Norman Wesley Gimbert II

Thesis submitted to the Faculty of the Virginia Polytechnic Institute and State University in partial fulfillment of the requirements for the degree of

Masters of Science
in
Aerospace Engineering

Joseph A. Schetz, Chair
Roger L. Simpson
Richard W. Wlezien

August 28, 1997
Blacksburg, VA

Keywords: Separated Flow, Detector, Aircraft

Development of a Sensor for Inflight Detection of Three-Dimensional Flow Separation on a Wing

Norman Wesley Gimbert II

(ABSTRACT)

A real need exists for a sensor capable of detecting flow-field separation on an airplane wing during routine flight operations. A sensor of this type could lead to both improved flight safety and increased performance. It would also contribute to future separation control technologies. A new idea is presented for a sensor that is cost effective, easy to maintain, durable, and highly effective. The system, known as a Thermal Grid, works by using a grid of heaters and temperature sensors to trace out the streamlines closest to the surface. Specific singularities in these streamlines are excellent indicators of flow separation. This paper addresses many of the necessary principles that are necessary to making the Thermal Grid an operational device. An analytic design is presented that details the system requirements and potential performance, including heater/sensor spacing, heater power requirements, sensor time response and sensitivity needs and the effects of changes in flow conditions.

Dedication

This paper is dedicated to all those who have helped me along the way. This includes my friends, my immediate and extended family, the members of my church, and especially my wife.

Acknowledgments

I would like to thank all those who have provided the assistance, and the expertise, and given me direction. This include Dr. Schetz, my advisor, who has treated me as an equal. The new ideas in this paper came out of a series of give and take brainstorming sessions between Dr. Schetz and myself. I would also like to thank Dr. Wlezien, who first introduced me to the real side of experimental aerodynamics when I worked under him at NASA Langley. Further, it was his faith in my abilities that made this work possible. I would also like to thank Dr. Fay Collier who was my first mentor at Langley and whose patience with my constant questions and requests for assistance is deeply appreciated.

This work was also made possible by all those who have given their advise, technical expertise, and necessary raw materials. This include Sandia National Labs who generously donated an 8 foot span extruded aluminum wing from which the wind tunnel models were made. I would also like to thank Dr. Olsman who taught me the technique, the method, and provided many of the materials for the oil flow experiments. Alex Marshakov, who had earlier worked with Dr. Schetz on the skin friction gages, was instrumental in the redesign of those gages for this purpose and who put in many long hours as we conducted the experiments in the stability tunnel. The other faculty that have provided valuable help in this endeavor include Dr. Simpson and Dr. Mason.

Lastly and most importantly I would also like to thank my wife. She has supported me when I needed it, and pushed me when I needed that instead. In this endeavor her help has been immeasurable.

TABLE OF CONTENTS

LIST OF VARIABLES ..... ***vi***

LIST OF FIGURES ..... **viii**

CHAPTER 1 INTRODUCTION **1**

CHAPTER 2 *INITIAL WIND TUNNEL TEST SERIES* **9**

INTRODUCTION 9
WIND TUNNEL 9
MODEL 10
INSTRUMENTATION 12
RESULTS 14

CHAPTER 3 THE THERMAL GRID **18**

CHAPTER 4 OPEN JET TUNNEL TEST **24**

INTRODUCTION 24
WIND TUNNEL 25
MODEL 26
INSTRUMENTATION 28
RESULTS 29

CHAPTER 5 *ANALYTIC DESIGN STUDY* **32**

CHAPTER 6 *PRELIMINARY DESIGN OF A THERMAL GRID* **50**

CHAPTER 7 *CONCLUSION* **55**

REFERENCES **56**

APPENDIX A *MATLAB CODES* **58**

List of Variables

τ	Temperature Sensor Time Response
T	Temperature at a point
T_{ave}	Average Temperature over Sensor
$\hat{T}$	Temperature at a point in the Fourier Domain
x	Axis coordinate in the streamline direction
z	Axis coordinate in direction of the outward normal
y	Axis coordinate to complete right-handed x, y, z coordinate system
U	Velocity component in x direction
V	Velocity component in y direction
W	Velocity component in z direction
U_e	External streamline velocity (Outside of the Boundary Layer)
$\overline{U}$	Effective convection velocity
$\overline{K}$	Ratio of ν_T / Pr_T, also known as thermal diffusivity
ν_T	Turbulent kinematic viscosity
Pr_T	Turbulent Prandtl number
w_x	x-axis in Fourier domain
w_y	y-axis in Fourier domain
w_z	z-axis in Fourier domain
t	time
x_c	x coordinate for sensor center
y_c	y coordinate for sensor center
w	Sensor physical dimension
t_h	Time it takes for a parcel of heated fluid to cross over heater
P	Heater Power Output
q	Sensor Output
w_h	Heater physical dimension

Q	Temperature to which amount of heat released would raise a unit volume of air
E	Amount of energy released by a heater
u^*	Dimensionless Boundary Layer Velocity
z^+	Dimensionless Boundary Layer Distance normal to surface
ν	Kinematic viscosity
X_{LE}	Chord-wise distance from wing leading edge
t_n	Dummy variable of integration
Θ(s)	Sensor Output in Laplace domain
$\overline{T}_{ave}(s)$	Average Temperature over Sensor in Laplace domain
q	Temperature to which amount of heat released would raise a unit volume of air per unit time
C_P	Specific Heat for air
ρ	Density of Air
φ	Angle in first quadrant of heated mass trail referenced from horizontal
S	Distance in both x, and y direction located between Sensor centers
Pe	Peclet Number
D	Worst case distance between heated mass trail and closest sensor for all angles
i	Indexing variable

List of Figures

FIGURE 1-1 TWO DIMENSIONAL FLOW SEPARATION 4
FIGURE 1-2 3-D FLOW SINGULARITIES 6
FIGURE 1-3 SEPARATION ON A FINITE WING WITH AN ASPECT RATION OF 4.8, A MACH NO. OF 0.7 AND AN ANGLE-OF-ATTACK OF 6 DEGREES 6
FIGURE 1-4 SKETCH OF SEPARATION AT HIGH INCIDENCE....7
FIGURE 1-5 SKETCH OF TRANSONIC WING SEPARATION PATTERNS 8
FIGURE 2-1 VIRGINIA TECH STABILITY TUNNEL LAYOUT 10
FIGURE 2-2 NACA 0015 WING MODEL 11
FIGURE 2-3 LOCATION OF SKIN FRICTION CUTOUTS ON WING MODEL 13
FIGURE 2-4 OIL FLOW PATTERN PRODUCED AT 15 DEGREES ANGLE OF ATTACK 15
FIGURE 2-5 OIL FLOW PATTERN PRODUCED AT 16 DEGREES ANGLE OF ATTACK 15
FIGURE 2-6 OIL FLOW PATTERN PRODUCED AT 17 DEGREES ANGLE OF ATTACK 16
FIGURE 2-7 OIL FLOW PATTERN PRODUCED AT 18 DEGREES ANGLE OF ATTACK 16
FIGURE 3-1 GRAPHICAL REPRESENTATION OF ONE ELEMENT OF A THERMAL GRID 19
FIGURE 3-2 SIMPLE REPRESENTATION OF THE THERMAL GRID 19
FIGURE 3-3 THERMAL GRID IN A PARALLEL PROCESS 20
FIGURE 3-4 THERMAL GRID REFINEMENT FOR RELIABILITY....20
FIGURE 3-5 BENEFIT OF INCREASED SENSOR DENSITY....22
FIGURE 4-1 VIRGINIA TECH OPEN JET TUNNEL 25
FIGURE 4-2 TEST BED MODEL IN OPEN JET TUNNEL TEST SECTION 27
FIGURE 4-3 PLOT OF RELATIVE TEMPERATURE AS MEASURED BY A THIN FILM RTD FOR 50V DC RTD HEATER 1 IN. UPSTREAM 31
FIGURE 5-1 AVERAGE SENSOR TEMPERATURE (°F) AS A FUNCTION OF SENSOR CENTER POSITION RELATIVE TO THE HEATER AT TIME=0.057S FOR CASE A 36
FIGURE 5-2 AVERAGE SENSOR TEMPERATURE (°F) VS. TIME (SEC.) FOR A FIXED SENSOR LOCATION FOR CASE A 37
FIGURE 5-3 PEAK SENSOR TEMPERATURE (°F) AS A FUNCTION OF SENSOR CENTER POSITION RELATIVE TO THE HEATER FOR CASE A 38
FIGURE 5-4 PEAK SENSOR TEMPERATURE CONTOURS (°F) AS A FUNCTION OF SENSOR CENTER POSITION RELATIVE TO THE HEATER FOR CASE A 39
FIGURE 5-5 PEAK SENSOR TEMPERATURE (°F) AS A FUNCTION OF SENSOR CENTER POSITION RELATIVE TO THE HEATER FOR A MODERN TRANSPORT AIRCRAFT AT IT'S LANDING CONDITION (CASE B)....40

FIGURE 5-6 SENSOR OUTPUT (°F) VS. TIME (SEC.) FOR A FIXED SENSOR LOCATION WITH τ = 0.01 SECONDS FOR CASE A.....42

FIGURE 5-7(A) PEAK SENSOR OUTPUT CONTOURS (°F) FOR τ = 0.1 SEC., AS A FUNCTION OF SENSOR CENTER LOCATION RELATIVE TO THE HEATER FOR CASE A 43

FIGURE 5-7(B) PEAK SENSOR OUTPUT CONTOURS (°F) FOR τ = 0.01 SEC., AS A FUNCTION OF SENSOR CENTER LOCATION RELATIVE TO THE HEATER FOR CASE A 44

FIGURE 5-7(C) PEAK SENSOR OUTPUT CONTOURS (°F) FOR τ = 0.001 SEC., AS A FUNCTION OF SENSOR CENTER LOCATION RELATIVE TO THE HEATER FOR CASE A 44

FIGURE 5-7(D) PEAK SENSOR OUTPUT CONTOURS (°F) FOR τ = 0.0001 SEC., AS A FUNCTION OF SENSOR CENTER LOCATION RELATIVE TO THE HEATER FOR CASE A 45

FIGURE 5-8 PEAK SENSOR OUTPUT VS. TIME RESPONSE FOR A FIXED SENSOR LOCATION FOR CASE A 45

FIGURE 5-9 PEAK SENSOR TEMPERATURES (°F) AS A FUNCTION OF SENSOR CENTER LOCATION RELATIVE TO THE HEATER AT TIME (TIME = ∞) FOR A CONTINUOUS HEATER FOR CASE A.....47

Chapter 1 *Introduction*

The problem of flow separation on the wing of an aircraft is an old and persistent one. It's difficulty was well summarized by A.M.O. Smith[1] when he wrote,

> "In a "hard" science one could treat the problem by giving a few equations that covered a certain class of phenomena… There are other sciences which are mainly descriptive. Unfortunately, the special science of stall [separation] and buffeting lies mostly in this latter class, meaning there are only a few facts that can be covered with any semblance of a law."

One of the primary issues is predicting the transition location, which in large part determines the thickness of the boundary layer. Transition prediction is made difficult because of the unsteadiness of the flow, and because of sensitivity to heating and surface roughness[2]. Even if transition is accurately predicted, the complexity of boundary layer separation adds to the problem. Flow separation is complex even in steady two-dimensional cases. This complexity is because the underlying turbulence is always three-dimensional and highly unsteady. Separation, unlike many other areas of fluid dynamics, lacks a unifying principal, and the science is mostly a collection of isolated experiences. Thus engineering prediction is difficult despite the enormous amount of data[1].

Separation affects both commercial and military aircraft. On commercial transports, areas include the high lift system, buffet margin at cruise, and increased drag[2]. Poor stall characteristics can endanger both the crew and passengers[3]. The military can face similar issues especially for transports performing high 'g' maneuvers without buffet, and by limiting the allowable angle of attack[2] for high performance aircraft. The issue of aircraft aging is also important in that repairs and even original construction will tend to deviate the aircraft from the exact configuration as tested during flight tests. This can lead to small undetected areas of separation that affect drag and performance[4]. A system that would monitor such flow separation could alert maintenance crews and allow the problem to be corrected. Larger areas of separation can lead to buffet, which can cause

considerable discomfort for passengers as well as structural fatigue[2]. A whole new set of problems can occur in the transonic regime if the shock strength is sufficient to separate the boundary layer. It would be possible to provide an early warning and give the pilot time to move away from the dangerous condition if flow separation could be detected in it's early stages. Any warning the pilot can receive will improve both safety and performance.

Current methods of handling the problem of separation primarily avoid the operating conditions where the wing would be vulnerable. Alternatively, modifications are made to the wing when the first method isn't satisfactory. The primary means of avoiding the separation onset is by limiting the aircraft's allowable angle of attack. This isn't always practical due to large gusts, and the limitation it places on $C_{L,max}$. $C_{L,max}$ can be increased by vortex generators, fences, leading edge extensions or slats, and stall strips, which are typical on just about every modern jet transport[5,3]. While these modifications work, they also produce unwanted effects usually by increasing drag at some stage of the flight where they are not needed[3]. A separation sensor would enable retractable devices that are deployed in the flow only when required.

The careful design of airfoils with tailored pressure distributions and large leading edge radii will ensure that the separation development process will be slow from trailing edge forward[5]. This produces a characteristic nose down pitching moment, permitting the pilot to move away from the condition. However, Shevell[3] notes that during the development of the DC-9 it was necessary to add tab-type angle of attack sensors, because the aerodynamic stall warning proved to be insufficient. These are an imprecise method of monitoring separation at best. It should also be noted that thick leading edges can produce increased drag creep at high speeds and lower drag divergence Mach numbers at low lift coefficients[2].

While these methods have worked well in providing safe aircraft, they are not without additional problems. It is impossible to fully account for ice, rain, or gusts which

can cause separation to occur under the right conditions,. Large margins of safety built into the airfoil and control system design sacrifice performance. A system which could detect the onset of separation in real time and provide warning to either the pilot and/or a Flight Management System[4] could increase safety while reducing the constraints on designers.

Further in the future, it may be possible to control separation in an active sense by blowing, suction, or flow actuation. The ability to accomplish control over separation could have dramatic ramifications, from the elimination of heavy and complicated high lift systems to the ability to extend aircraft performance to high alpha without the need to resort to vortex flows and their associated increased drag. An important feature in any such system is likely to be a flow separation sensor that would be able to sense that separation is beginning, where on the wing it occurs and to what degree it occurs. Thus flow control could be accomplished in a closed-loop fashion.

This study will deal with such sensors. It is important to realize that for such a sensor system to be useful it must be applicable to real aircraft. This means that the sensor must be rugged and durable. It must also detect separation that occurs on finite wings, i.e., in three dimensional flows. In addition, the sensor must not disturb the flow, it must be reliable, fault tolerant, accurate, and cost effective. An ideal sensor would also be surface mounted with little intrusion into the interior of the wing, which is occupied by fuel tanks and other systems, so that installation on an existing aircraft would not require an extensive overhaul.

Flow separation occurs in the air stream above the wing and the sensor must not disturb the flow; thus the sensor must infer separation by means of measurable criteria on the wing surface. Flow separation is not a unique phenomena; it's form varies significantly depending on the geometry of the body. Classically, separation has been studied over wings with infinite span. This represents a two dimensional (2D) flow, and the surface criteria have been well understood since Prandtl[6] first studied it in 1904. At the point of

separation, the velocity gradient (and the skin friction) become zero and the flow near the surface reverses direction (termed "backflow[7]".") This can be seen in Fig. 1-1 as drawn by Prandtl.

Qualitatively, 2D separation is usually detected by surface flow visualization such as oil flow tests or tufts. The shear forces produced by the fluid will act upon the tracer and move it. In the region where backflow begins, the flow upstream of the region will push the tracer downstream, while the backflow will push the tracer upstream forming a line normal to the flow direction.

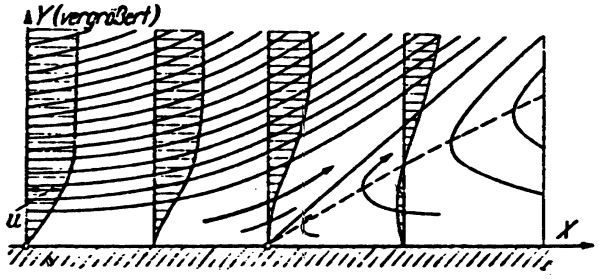

Figure 1-1 Two Dimensional Flow Separation[6]

The skin friction or velocity gradient normal to the surface can be measured to quantitatively determine the separation location. This criteria is most often used in numerical calculations, however it could be measured experimentally either directly, by use of a skin friction gage, or indirectly, by measuring the heat flux and relating it to skin friction via Reynolds analogy. It should be noted that this measurement is difficult, because the skin friction tends toward zero at the separation location and is thus very small. The most frequent experimental technique attempts to measure the backflow by means of a thermal tuft[9,10,11]. A thermal tuft is a device used to measure backflow by placing sensors upstream and downstream of a wire heater slightly above the surface. A Wheatstone bridge compares the resistance of the upstream and downstream sensors to detect the direction that fluid heated by the central wire is being convected. A more complete review of 2D separation and methods for its detection was conducted by Simpson[7]. Also of interest is a 1977 patent by Mateer and Brosh[12] that proposes to use a

thermal tuft on operational aircraft. However, it should be noted that this technique can only reliably detect separation on unswept high aspect ratio wings. Even then, it will not work near the tips where 3D flows dominate. Separated regions in 3D flows often do not have any backflow. Further, a device with fine wires above the wing surface cannot be made robust enough for use on operational aircraft.

An examination of the process of three dimensional separation shows the conditions of zero skin friction and backflow are not sufficient or necessary[13]. A simplistic way to view separating flow is to say the flow approaches a "wall" of pressure and can either push the wall along with it or stop and jump the wall. However, if the wall is not infinitely wide (as in a three dimensional flow) the flow has the third choice of going around the wall.

In the search for a surface flow separation criteria for three dimensional flows, experience leads us to look closely at the limiting streamlines, which are the streamlines closest to the surface. Examination of numerous surface flow visualization pictures shows that a series of patterns in the limiting streamlines tend to occur in relation to the flow separation[14]. One can turn to the mathematical expansion of the limiting streamlines around a singularity in looking for an explanation for these patterns. This leads to several different patterns depending on the relative magnitude of the expansion coefficients. The dominant ones are shown in Fig. 1-2. Further examination of the relation between these patterns and separation shows that the line of separation is different from the other limiting streamlines in that it connects these singularities, while the other limiting streamlines simply connect to the separation line to one of these singularities[14].

The first of a series of examples that relate to our goal of understanding the separation on a finite swept wing can be seen in an oil flow photo obtained by Vanino and Wedemeyer[15] and a corresponding sketch by Wang[14] for a wing with an aspect ratio 4.8, tested at $M = 0.7$ and $\alpha = 6°$ as shown in Fig. 1-3. The separation line can be seen near the trailing edge as a series of nodal points. This seems to be typical of trailing edge

separation, which for subsonic flows is the first stage encountered as the incidence angle is increased.

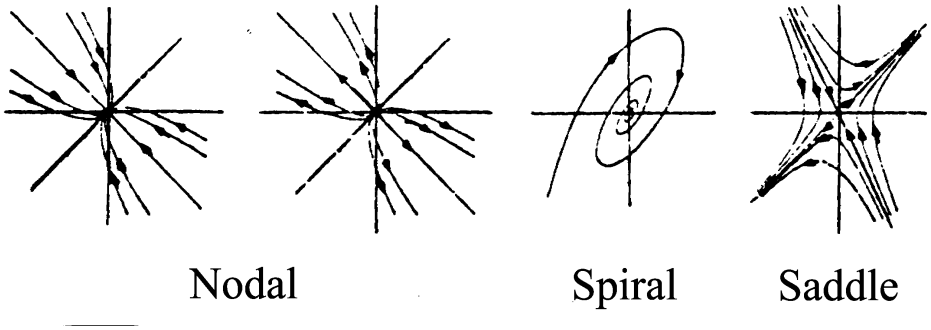

Figure 1-2 3-D Flow Singularities[14]

More recently this interpretation has been called into question. Yates and Chapman[21] note that for crossflow separations there are no three-dimensional critical points on the surface associated with separation. However, they also point out that downstream of the onset of separation there is a strong convergence of the limiting streamlines. Such a converge of the limiting streamlines can be noted in Figure 1-3 in what Wang termed as the line of nodal points. Regardless of the explanation the flow is the same, and it is clear that the onset of separation can be determined by the mapping of the surface streamlines.

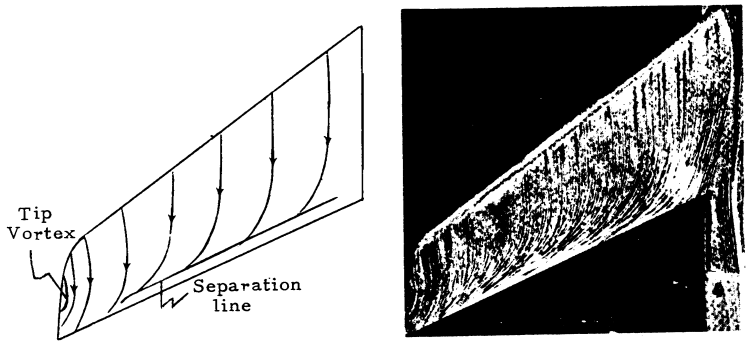

Figure 1-3 Separation on a Finite Wing with an aspect ration of 4.8, a Mach No. of 0.7 and an angle-of-attack of 6 degrees[14,15]

The next example shows that the character of the flow can change dramatically at higher angles of incidence. This can be seen in a sketch by Wang[14] in Fig. 1-4. Here, the

separation pattern consists of an inboard spiral vortex and an outboard saddle-like pattern. A vortex that develops at the spiral node can be seen to flow downstream above the wing's surface. While this represents an extreme case of separation, it demonstrates the consistency of this aspect of the 3D separation process.

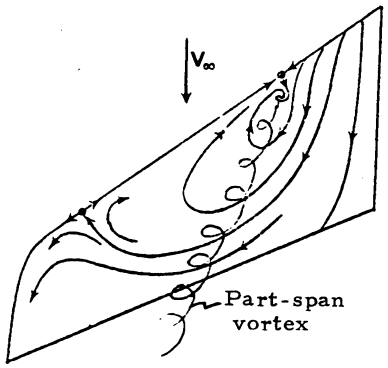

Figure 1-4 Sketch of Separation at High Incidence[14]

At transonic speeds, shock waves will begin to develop that will again change the character of the flow. A weak shock will cause a "kink" in the limiting streamlines, while at higher speeds the strong outboard shock of a 'λ' shock pattern can cause separation. This forms a series a nodal point singularities in the limiting streamlines. Inboard, the more basic trailing edge separation pattern of nodal points can be observed[14]. This pattern can be seen in the high speed separation oil flows by Vanino and Wedemeyer[15], and sketched by Wang[14] as seen in Fig. 1-5. These cases show that the presence of singularities in the limiting streamlines are perhaps a sufficient condition to determine separation for a wide range of cases[14]. Additional research shows that this also holds true for delta wing configurations[5,14]. A more complete proof of these concepts, as well as the mathematical basis for these singularities, is described in Tobak and Peake[16] along with other factors such as their structural stability and bifurcation.

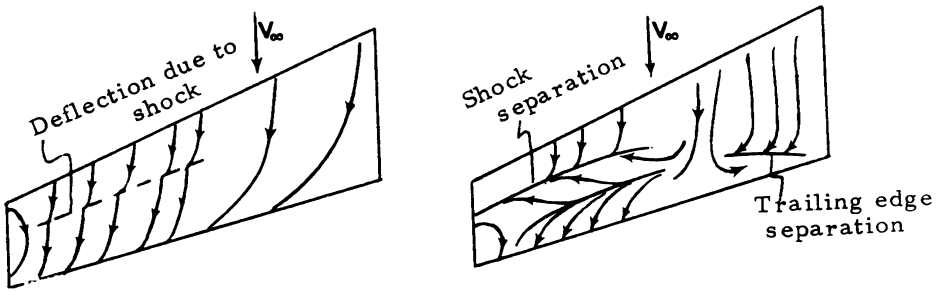

Figure 1-5 Sketch of Transonic Wing Separation Patterns[14]

The next logical question would seem to be how these lines could be traced by an operational sensor system. The most obvious answer is oil flows, as has been already shown. However, while oil flows can produce good results, they cannot be used in an active sense and are impractical for use on a real airplane performing day-to-day operations.

The limiting streamlines can be shown to be mathematically equivalent to skin friction lines[5]. So perhaps one could look for the convergence of the skin friction lines as a good indicator of singularities in the limiting streamlines, hence separation. This can be measured in the lab, but skin friction gradients must be measured all over the wing in sufficient resolution, and this is a costly and time consuming process. This is infeasible in the world of real airplanes with unsteady flow. This study will attempt to lay out the basic concepts of a new method. This proposed system of sensors referred to as the "Thermal Grid" takes advantage of the limiting streamline criteria and can be used to detect separation on an operational aircraft wing.

The remainder of this report is organized into several sections describing the initial wind tunnel tests in the Stability Wind Tunnel, a second test series in the Open Jet Wind Tunnel, and an analytic design study for a Thermal Grid. The last sections contain recommendations and conclusions.

Chapter 2 *Initial Wind Tunnel Test Series*

Introduction

The primary goal for the work was to develop an improved, first-hand understanding of the nature of the problem. Since numerical calculations for 3-D separated flows are currently expensive and unreliable, a wind tunnel investigation is the best course of action. The first test was not focused on a single experimental technique, because we were not confident what the best method would be. In this spirit, we conducted skin friction measurements and two forms of flow visualization- tufts and oil flows.

Wind Tunnel

The Virginia Tech 6ft. x 6ft. Stability tunnel is a continuous, closed jet, single return subsonic tunnel that was donated to Virginia Tech by NACA Langley in 1958. The tunnel is in excellent condition because the 600 hp d.c. motor was completely overhauled and the windings were reinsulated in 1994. The blades for the 14 foot prop were replaced in late 1996. In addition, the drive system was replaced in 1986 with a customized Emerson drive that allows for precise speed control with reduced vibration, and minimizes the cyclic unsteadiness inherent in older drive systems. The net result is excellent flow characteristics. The test section is 24 feet long with a rectangular, 6 foot by 6 foot, cross section. The tunnel is capable of a maximum speed of 275 ft/s. A general layout of the tunnel in shown in Fig. 2-1.

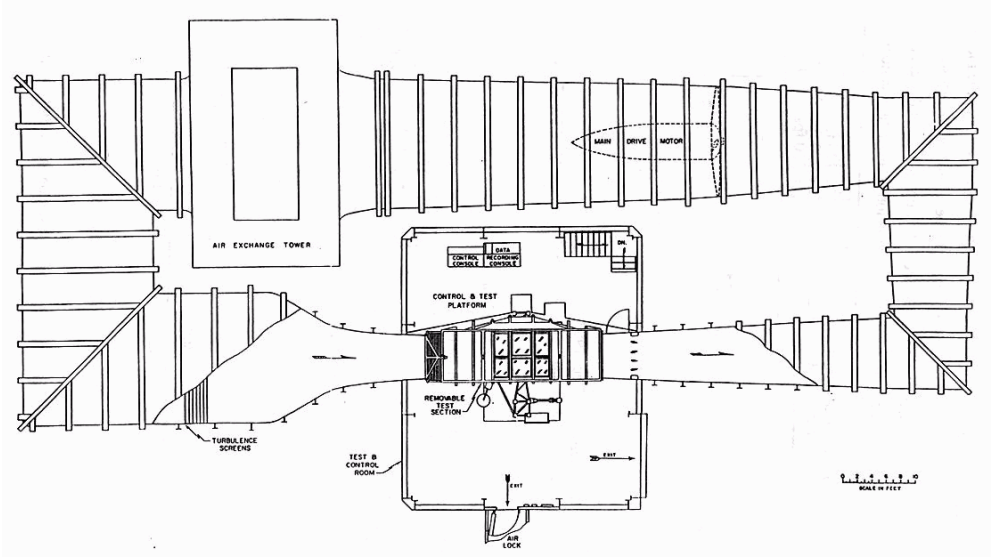

Figure 2-1Virginia Tech Stability Tunnel Layout

Model

A finite swept wing was placed in the Virginia Tech 6ft. x 6ft. Stability Wind Tunnel. The particular airfoil section was not critical, since we were investigating general separation patterns not specific to any particular wing. It was necessary to limit the model semi-span to 4 feet due to interference effects with the tunnel walls. Thus, the chord dimension would need to be a balance between aspect ratio and chord Reynolds number. It was also decided that the Reynolds number was more important based on the previous experiments by Wedemeyer and Vanino[15] who noted during their investigations of several wings, that aspect ratio played a minor role in the development of limiting streamline singularities. So a large chord model was required. A suitable model was a 2 foot chord, 8 foot span, extruded aluminum NACA 0015 that was donated by Sandia National Laboratories. This saved the cost and effort that would have been associated with building a new wing. A 15° sweep angle was chosen as representative. The NACA extrusion was modified by cutting the ends at 15° angles with a 4 foot semi-span. This resulted in a simple wing of constant airfoil section with no twist, taper, or camber, with a

sweep angle, Λ, of 15° and an aspect ratio, AR, of 4. A rounded cap was constructed out of foam and then smoothed over with polyester resin to close the free end. A 2 in. wide boundary layer trip of glass beads was used, beginning around 5% chord, on both the suction and pressure sides of the wing to insure a fully turbulent flow. A picture of the model taken after the tests can be seen in Fig. 2-2.

Figure 2-2 NACA 0015 Wing model

The floor section of the tunnel immediately over the tunnel turntable was removed to accommodate the model. The turntable is located beneath the center of the test section, about 2/3 of the length from inlet. The wing was bolted to a 1 in. thick, 26 in. diameter aluminum plate. This plate can be seen attached to the wing in Fig. 2-2. The plate was aligned with the floor of the test section by supporting it with three 1 in. diameter and 8 in. long steel rods that were arranged in a tripod fashion. At the bottom of this tripod, another 1 in. thick, 26 in. diameter aluminum plate was attached to the electric turntable that was controlled from the tunnel main control panel. A thin steel plate was cut to match the removed floor panel and a 26.25 in. hole was cut into it. This was placed where the floor section had been, aligned with the top aluminum plate of the wing support. This floor plate is also seen in Fig. 2-2. The 1/8 in. gap around the circular plate allowed the

wing to rotate freely, thus changing angle of attack. Since the chamber that surrounds the test section is sealed it achieves the same pressure as the test section, so leakage from this gap was not an issue. The tests were run at a free stream velocity of 202 ft/s corresponding to $Re_c = 2.5 \times 10^6$. This is a sufficiently high Reynolds number for reasonable airfoil tests.

Instrumentation

The tests that were originally envisioned included skin friction measurements, traditional tufts and TiO_2 (titanium dioxide) Oil Flows. The skin friction measurements were performed using an extension of the skin friction gages, used by Schetz and Marshakov[8] in a turbine blade, modified with a larger sensor head and a longer cantilever arm in order to measure the smaller forces associated with this subsonic flow. This is most clearly seen in the approximation for turbulent skin friction developed by Schultz and Grunow[13] which shows the skin friction coefficient is inversely related to approximately $U_e^{1/4}$. Since the coefficient is related to the shear force linearly with U_e, it can be deduced that the skin friction shear force will generally increase with $U_e^{3/4}$. The larger head allowed a larger area for the skin friction to act upon producing larger forces in the instrument, however it also averaged the measurements over a larger area reducing the precision when the friction varies sharply over the sensor. The longer lever arm increased the deflection produced by the skin friction. This deflection is detected by the strain gages in the unit. The primary drawbacks for this application include unit size, which prevented the sensor from fitting close to the trailing edge. In addition to the fact that without a dramatic increase in depth produced by placing the lever arm normal to the surface, the sensor is unable to measure more than one force component. The sensors were placed as close to the trailing edge as space permitted to see what could be learned. Six cutouts were made in the wing to install the gage, and the gage was moved between locations during the sequence of tests. The remaining cutouts were covered with aluminum plates that were shimmed in place. The edges of these plates were then smoothed by filling the

steps and gaps with clay. Since the airfoil section is symmetric, these cutouts were made on the side of the wing away from the windows. Flow visualization experiments could thus be performed on the side without the small disturbances likely produced by the cutouts while maintaining the view from the control center. The suction and pressure sides could be reversed by using negative angles of attack. The location of these cutout can be seen in Fig. 2-3

The tufts were made using strands of yellow cotton yarn about 1 in. long attached with transparent tape in 5 rows, starting at the trailing edge and moving forward. The tuft patterns were video taped for later viewing.

The oil flows were performed using a mixture of oleic acid, kerosene, and TiO_2. The mixture was painted in a thin layer over a sheet of black Frisk Coverseal that was attached to the suction side of the wing. After a test was completed, a clear flat overcoat was applied to the oil to fix the resulting pattern. The Coverseal was then removed and replaced with a clean sheet for the next test. Each of these tests were performed in increments of 1° angle-of-attack, from the angle of the initial onset of separation until the separated flow dominated the wing. The skin friction gages were at fixed locations on the wing, so the oil flows were used to attempt to perform measurements with the separation line progressing over the sensor.

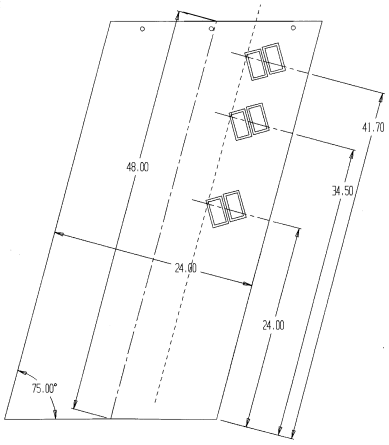

Figure 2-3 Location of Skin Friction Cutouts on Wing Model

Results

The results from the tests were mixed. The skin friction gage results were not useful. This was a result of only one force component being measured, whereas two are really essential for this flow problem. The second reason is that the larger angles-of-attack necessary for the separation line to reach the sensor also produced violent buffeting that shook the model. At this condition, the inertial loads on the sensing head dominated the small frictional forces being measured. If a skin friction gage could be developed that would measure two force components while being thin enough to fit in a wing model, this method might warrant a second look.

The tufts produced what originally seemed like realistic results. However, comparison of the observed patterns with the oil flows showed that similar flow separation occurred about 5° before that in the oil flow case. It is assumed that the thickness of the yarn and the tape probably caused premature separation. This highlights the extreme sensitivity to conditions that makes separation so difficult to predict.

The oil flows produced good results, showing patterns similar to those from other workers. The first signs of separation in the oil flows began at 15° angle of attack. A photo of the oil flow at this condition is shown in Fig. 2-4(a). In this and all subsequent oil flow pictures, the trailing edge is to the left, and the flow is from right to left. The deep white straight line towards the back is the paper backing the Coverseal. The edge of the Coverseal was aligned straight and flush with the trailing edge during the actual test. A closer look at the separated region is shown in Fig. 2-4(b).

Towards the top of the oil flow image the tip vortex can faintly be seen. The separated region can be seen form about one-quarter span to three-quarter span at the trailing edge. The various types of singularities are clearly visible, with a line of nodal points along the separation line moving up into a spiral singularity. As the angle of attack progresses, the separated region becomes larger. This can be seen by observing the oil

flows at 16° angle of attack as seen in Fig. 2-5. Another spiral singularity also begins to form while the initial one grows in size.


(a)

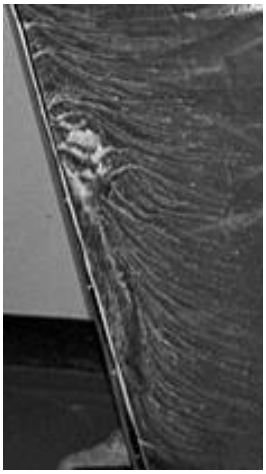
(b)

Figure 2-4 Oil Flow Pattern produced at 15 degrees angle of attack


(a)


(b)

Figure 2-5 Oil Flow Pattern produced at 16 degrees angle of attack

Note the marked difference between Fig. 2-5 and Fig. 2-4, considering that the only difference is 1° angle of attack. The progression continues into Fig. 2-6, (a) and (b), where the oil flow images are at 17° angle of attack.


(a)
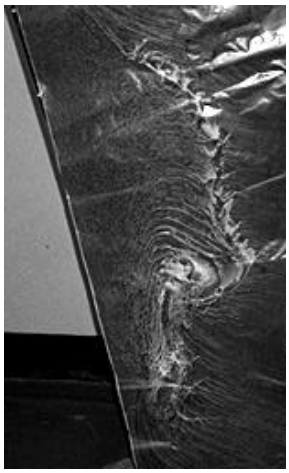
(b)

Figure 2-6 Oil Flow Pattern produced at 17 degrees angle of attack

Both spiral singularities continue to grow in size as they move further upstream. The tip vortex also appears at the top of Fig. 2-6(a), and the separated region consumes almost half chord around midspan. The last of these oil flow images is in Fig. 2-7 with the wing at 18° angle of attack. At 18°, the wing flow is consumed in a massive spiral vortex. The only flow features that remain are the tip vortex and the massive separation singularity.

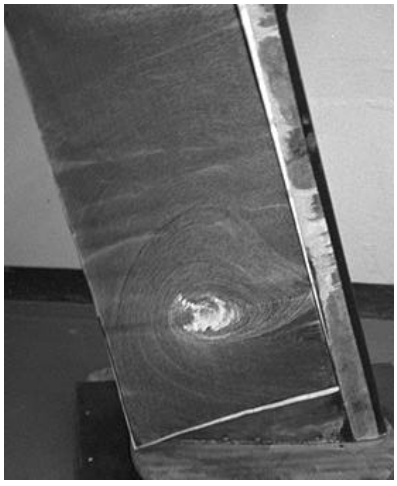
(a)
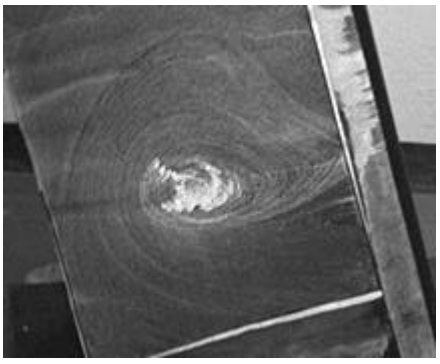
(b)

Figure 2-7 Oil Flow Pattern produced at 18 degrees angle of attack

Note that the entire progression from when separation was first detected at the trailing edge to the last case of massive separation only covers 3° angle of attack. This shows again the alpha sensitivity inherent in these flows.

Although these patterns are not identical to those described earlier, they are similar in that the separated flow can be characterized by the same types of singularities. A high Reynolds number test bed has been developed, and separation patterns have been recorded at a progression of angles of attack. This proved to be essential to prototype testing, when the building blocks of a working sensor were established.

Chapter 3 The Thermal Grid

It was clear after the initial tests that old ideas of detecting 2D separation would not work for cases where 3D flow dominates, as for a finite wing. Instead of simply measuring backflow, it is necessary to map out the limiting streamlines in the region where 3D separation might be expected. The expected flow pattern in this region would be determined for a particular wing configuration in the wind tunnel, and other tests would be performed beforehand. We began to search for ideas that might develop into a workable sensor capable of accomplishing this goal, using present day technology in a cost effective manner. We developed a concept called the Thermal Grid. The Thermal Grid is a grid of inexpensive heaters and temperature sensors with one, the other, or both located at each node of the grid. The underlying principle is that when a heater produces a burst of heat, the resulting heated mass is carried along with a streamline close to the surface. Temperature sensors are located at the nodes surrounding the heater, with the nodes spaced such that the heated mass can be detected before it leaves the perimeter. One element of such a configuration can be seen in Fig. 3-1. Taking the information of which sensor(s) detected the heated mass, how much heat was detected by each sensor, which heater it was emitted from, as well as the amount of heat released, the direction the heated mass was convected can be determined. This physical principal of a single element of the proposed Thermal Grid has some similarities to that of a Thermal Tuft. However, here the temperature sensors would each measure temperature absolutely, as opposed to differentially. This makes the logic of the system more complicated, but adds increased capability. In the case where the heated mass would pass between two sensors, diffusion would spread the heated mass and allow portions of it to be detected on either side. The relative balance of the heat to either side can provide a reasonable approximation of the limiting streamline direction.

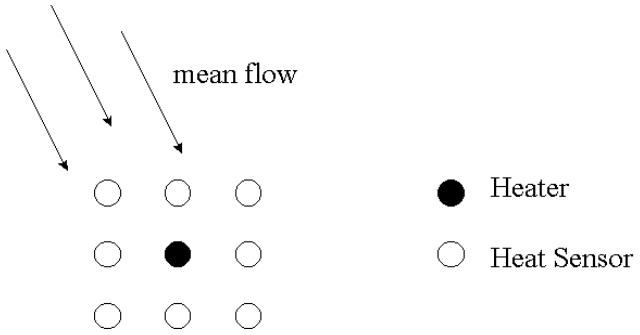

Figure 3-1 Graphical representation of one element of a Thermal Grid

Elements such as this are then be stacked to give a good baseline example of a working Thermal Grid. Since the flow direction is not known beforehand, the heater/sensor system should not be set up with any directional bias. For this reason the heaters and sensor should be either round or square. In this case, each node of the grid will contain both a heater and a sensor, with each node behaving as one or the other at any instant in time. The spacing of the nodes is equal in both surface dimensions, such that the heated mass will decay beyond detection just beyond the distance of the diagonal of the resulting square. The process would begin with the first heater releasing a burst of heat. That heat will be detected by a temperature sensor in the area where the limiting streamline carries it. At this point, the next heater, located at the same node as the detecting sensor, will release it's own burst of heat and the process will be repeated. This process is envisioned in Fig. 3-2. In the figure, the white circles are the heat sensors and the black dots represent heaters that were momentarily triggered.

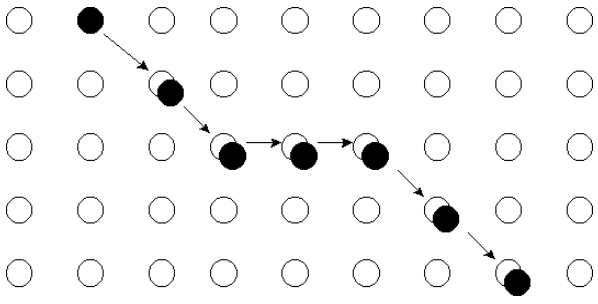

Figure 3-2 Simple representation of the Thermal Grid

This process will effectively trace a limiting streamline in an simple, rugged, and non-invasive manner. If multiple streamlines were traced, the types of singularities that would denote separation, such as nodal and spiral points, could be observed. Prior knowledge of the expected flow pattern would give clues as to what type of singularities would be expected. The sensor system could accomplish the identification through the use of a Neural Network that has been trained to recognize these patterns.

The general notion of the Thermal Grid is much more extensive than the above baseline description from which more complicated versions can be developed. Some of the more obvious modifications can be made to increase both the speed at which information on the flow field is obtained and the reliability with which the system will operate. In addition, analysis might also show that a nodal pattern different from the baseline square might be more optimal. The best method for increasing the speed of information collection would be the ability to track more than one heated mass at a given instant in time. Since the process of separation is so sensitive, this parallel processing would be essential for the timely detection of onset. The primary consideration necessary for such a capability would be to avoid confusion of the various signals. This would lead to one of two possibilities. The first is simply to space the active heaters far enough apart such that the paths of the heaters would not overlap. A demonstration of this can be seen in Fig. 3-3.

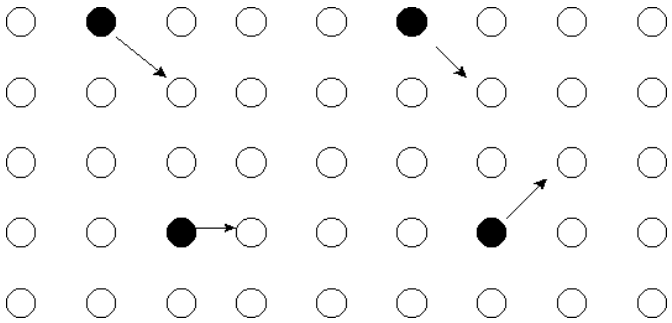

Figure 3-3 Thermal Grid in a Parallel Process

The other option would require the ability to distinguish one heated mass from another, perhaps by varying the pattern with which the heat is released. This capability would require both heaters and temperature sensors with fast time responses.

The second refinement would be to space the sensors such that two or three temperature sensors fit within the distance it takes the heated mass to fully diffuse. See Fig. 3-4.

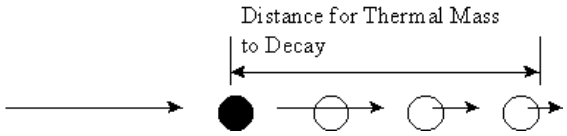

Figure 3-4 Thermal Grid Refinement for Reliability

While this would increase the total number of sensors used within the system, it would also considerably increase the system reliability. Since the baseline system would involve a large number of sensors, the probability of any one sensor failing would not be unreasonable over the life of an aircraft. In the baseline configuration, loss of one sensor could result in a lost signal that would be detrimental to the timely detection of separation. Fitting more sensors in the same space, while increasing the probability that any one sensor might fail, would dramatically decrease the probability that all the sensors in the path of a heated mass would fail, thereby preventing the loss of a signal. The monitoring computer system could easily detect which sensors repeatedly fail to respond. This would speed repairs and lower the operational cost of the system. Increasing the number of sensors would also refine the resolution, and thus the degree of curvature, of the patterns the system would be capable of tracing. It would also decrease the need for inferring the direction of a heated mass that passes in between two sensors. If the heat passes in between two sensors in the first row, the angles work out so that it is more likely to hit a sensor in the second or third row. This can be seen in Fig. 3-5.

While the benefits of increased sensor density are clear, this would also make the system more complex and expensive. Providing that sensors with adequate performance

can be purchased or manufactured at an affordable cost, the sensor density can be decided in the final analysis. It should also be noted that in this situation, there no longer needs to be a heater at every node in the grid, as in the baseline case.

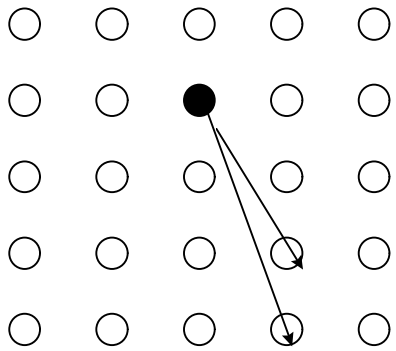

Figure 3-5 Benefit of Increased Sensor Density

Besides the obvious spacing question and the decision of which of the devices should be placed at a given node, there are numerous other variables that need to be considered for a real system. For the heater these include size, power rating, and temporal response to maximum temperature. The temperature sensor will also have requirements. Including sensor size and time response. Effects like the efficiency of heat transfer from the heater to the air stream, the length of time of the heat burst, as well as the thermal conductivity of the substrate material will also need to be studied. It is also important to consider the ability of the devices to withstand the harsh external conditions, from rain to sleet to icing, all at very high speeds. Since the devices are likely to be located around the trailing edge, they should not take maximum loads. However, they will need to be very robust. One of the most difficult balances is likely to be the need for rugged devices as well as for fast time responses. In general, it holds that smaller devices are more fragile and have less thermal inertia. A low thermal inertia is equivalent to a fast time response.

In making the Thermal Grid a reality, these and many other question need to be addressed. Additional difficulties will include the wiring of a large number of sensors as well as the development of the logic to run the system and to interpret the results in real

time. While this is likely to be a computationally intensive task, the ever increasing speeds of modern computers should be able to address this last issue. With all this considered, it is clear that the Thermal Grid is capable of becoming a cost effective, high speed, rugged, noninvasive means of detecting 3D separation of the type that occurs on an aircraft wing.

Chapter 4 Open Jet Tunnel Test

Introduction

Following the formulation of the principles behind the Thermal Grid, it was determined that a more affordable means of system development was needed. While the stability tunnel performed well in the earlier tests, the costs that would be associated with an ongoing sensor development program was prohibitive. This led to the development of a second test bed that could be used in the Virginia Tech Open Jet Tunnel. This enabled evaluating various systems in a real flow and debugging any system troubles without the pressures of work in a full-scale tunnel environment. Since the open jet tunnel is primarily used for undergraduate labs at Virginia Tech and has generally poor flow characteristics, it is often left unused and has no associated run time costs. It was decided to use this model to attempt to simulate the most fundamental process of the Thermal Grid, i.e. passing a burst of heat from a heater to a temperature sensor downstream. While this process has been performed many times with Thermal Tufts, this experiment involved attempting this process using inexpensive Resistive Temperature Devices or RTDs as opposed to much more sensitive fine wires. These devices have several advantages for application to a Thermal Grid. Primarily, they are inexpensive, small, durable, and their accuracy is very stable over long periods of time. All these are essential elements for the sensing element in a Thermal Grid. The other unique advantage of a RTD is that when a current is passed through one, it will act as an electric heater. This would be highly advantageous for the Thermal Grid because it would only require the installation of a single device at each node of the grid to get the functions of both the heater and the sensor. Such a feature could dramatically lower the total system costs for a Thermal Grid. This can be done because a node will only perform one of these two operations at a given point in time. The OMEGA[17] literature for thin film RTDs also indicated quick response times and a very

high destruction voltage. Also, oil flow tests were conducted to verify the flow features that might be examined in the future.

Tunnel

The Virginia Tech Open Jet Tunnel was designed and constructed by members of the Virginia Tech Aeronautical Faculty. The tunnel is an open-throat return type of tunnel with a 3-foot test section. It was constructed of plywood that was made smooth with shellac and varnish. The tunnel consists of a circular tube with diameter ranging from 39 in. to 72 in. It is powered by a 35 H.P. DC motor and uses a four-bladed Hartzell propeller. All this translates into a maximum tunnel speed about 150 miles per hour without blockage. A Pitot-static probe is connected to a water manometer graduated to read 0.01 in. H_2O, which is used to determine the dynamic pressure. A schematic of the tunnel can be seen in Fig. 4-1.

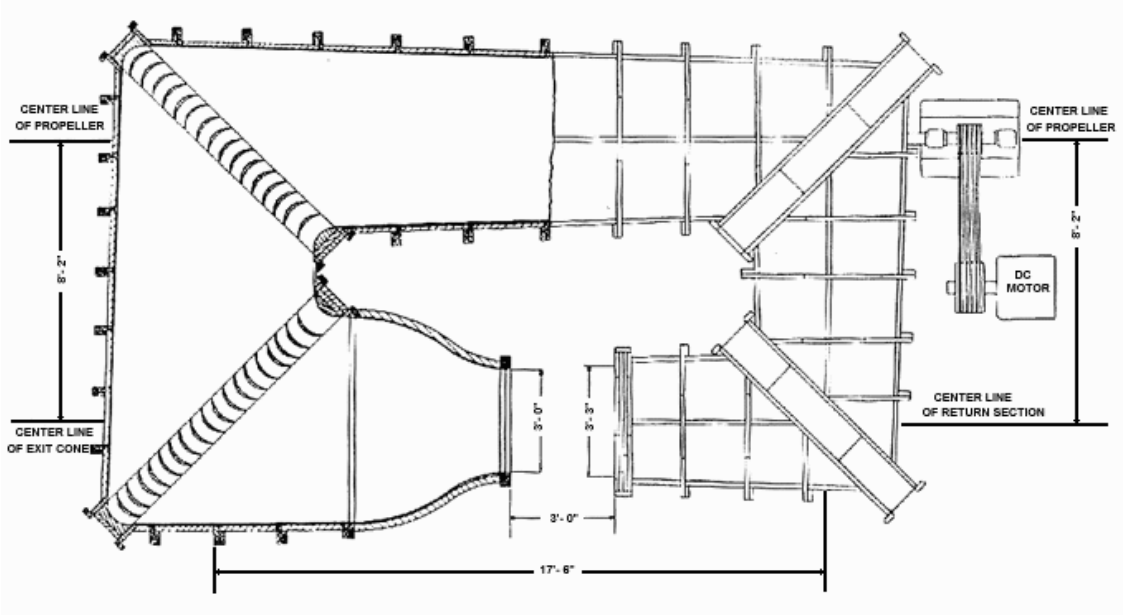

Figure 4-1 Virginia Tech Open Jet Tunnel

Model

The model used in the open jet facility was as similar as possible to the model developed for the stability tunnel. It was, therefore, decided to make use of the remaining piece of the extruded aluminum NACA 0015. The wing has a 2 foot chord and is constructed with ¼ in. aluminum skin and ¼ in. aluminum spars running the length of the wing. These spars, in effect, formed 5 chambers, each running the length of the wing. The 15° sweep was also maintained, as used for the stability tunnel model. Due to the limited test section size of the open jet tunnel, the model was limited to a two foot span. This resulted in an aspect ratio of 1. In order to limit the three-dimensional effects due to the low aspect ratio, it was decided to add end plates to both ends of the wing.

The endplates were each 30 in. in diameter and were constructed of 1/8 in. steel with rounded edges. An aluminum insert was cut to shape, inserted, and then bolted into the center most chamber in one end of the wing. The insert was tapped for a ½ in. thread. A 1 in. pipe was then threaded so as to screw into the insert perpendicular to the wing edge. This pipe had two purposes. One was to support the model and allow it to be rotated to various angles of attack. The second was to support the endplate. Four small screws were also screwed into the wing skin through the endplate to prevent it from rotating relative to the wing. This setup allowed the endplate to be removed, if necessary, while the pipe still supported the model. The wing end was sealed with duct tape for the case when the endplate was not attached.

On the opposite end of the wing, 4 taps were created at the four corners of the 2nd chamber from the front. An additional ½ in. tap was created at the trailing edge. These five holes were used to bolt the wing and the second steel endplate together at a given angle. A ½ in. x 1 in. x 6in. steel bar was then bolted to this second endplate with the long dimension perpendicular to the plate. Two cross bars were attached to the tunnel across either side of the test section. A clamp was attached to the center of one cross bar to accept the pipe and allow it to rotate while supporting the wing. The steel bar was then

bolted to the opposite cross bar. This held the endplate at a fixed angle and locked the wing into an angle relative to the endplate. This angle was defined by the position of the 5 holes in the endplate to which the wing was bolted. A series of sets of holes were created at various angles in the endplate to allow the wing to be bolted at multiple angles of attack. A set of 1 in. wide boundary layer trips were created from strips of a sanding belt and were taped near the leading edge to the upper and lower surface.

The model can thus be operated at a series of predefined angles of attack, both with or with out the endplate on the pipe end. A picture of the model installed in the test section of the open jet wind tunnel can be seen in Fig. 4-2. One can note in this figure that the removable endplate has been taken off. The trip strip, and pipe support, as well as the swept leading and trailing edge can also be observed.

Figure 4-2 Test Bed Model in Open Jet Tunnel Test Section

Instrumentation

The oil flows were conducted first. These were performed according to the same techniques used in the earlier stability tunnel tests as described in Chapter 2. The RTD setup involved several components. The RTDs themselves were actually know as TFDs or Thin Film Detectors as sold by OMEGA[17]. This device was chosen because it was cost effective, rugged, and small. The device measures the temperature by observing the resistance change of platinum which varies linearly with temperature and is very stable over a long period of time, even with rapid cycling. Because the Thermal Grid sensors will work independently, it is important for their output to not significantly differ from each other for the same input. OMEGA[17] claimed the TFD has an unspecified "fast" response time and a voltage necessary for destruction of 100V (DC).

The oil flows showed that the streamlines were straight near the center of the wing. The RTDs were placed along one of the visible streamlines with one 1 in. downstream of the other. They were attached to the wing with high temperature tape such that the wire connections pointed to the fixed endplate. The wire connects and wire edges were then smoothed over with a small amount of clay. The upstream RTD was set up to be used as a heater, and the downstream RTD was to be used as a temperature sensor. The upstream sensor was connected to a high voltage DC power supply through a 5v DC relay. The sensor RTD was connected to a constant current or trans-conductance amplifier. The amplifier worked by accepting a constant voltage input which was transformed into the constant current signal, with the output current directly proportional to the input voltage. In this case, the amplifier was setup such that 1v = 1.9mA. A feedback system monitored the current being drawn and rapidly acted to maintain it constant.

An IBM compatible PC was used to conduct the experiments. The PC was equipped with a DAS-20 D/A, A/D converter manufactured by Keithley-Metrobyte. The DAS-20 was controlled by means of the LabTech Notebook data acquisition software. A

routine was written that would output a voltage for the constant current amplifier; at the same time, it would trigger a 5v DC signal for the heater relay and then monitor the output voltage off of the sensor RTD. The constant current amplifier signal was set to 2v DC. This resulted in a sensor current of 3.8mA. It was necessary to use a buffer on both the 5v signal for the relay and for the DC volt signal for the constant current amplifier to not load down the D/A converter. The measured sensor voltage was directly related to the resistance, and thus the temperature, because of the constant current. During one test, a multimeter was installed along the current line to ensure that it stayed constant.

The test was run several times. The wing was set to 10° angle of attack, with the removable endplate taken off. The heater voltage was set to different values to determine how the RTD would perform under high voltage situations. The heater was originally set for 90v DC which is below the stated 100v destruction voltage. For some runs, the tunnel was on and for others the tunnel was off to ensure that the measured temperature wasn't merely being conducted through the aluminum wing. The tunnel-on cases were all run at the tunnel maximum speed. This was expected to be substantially reduced due to the fact that the large wing presented a considerable amount of blockage.

Results

The results from this test were mixed. The tunnel was run at about 81.7 ft/s. The heat produced from the heater was eventually detected downstream. The heaters effects on sensor output were minimal when the tunnel was off. This confirmed that the heat was convected by the air, and not conducted through the aluminum substrate. However, several key points were learned about the RTD. First, the listed 100v DC destruction voltage was far from accurate. When the heater was set to 90v the RTD was instantly destroyed. Later at 65v, the heater was also destroyed but only after several minutes of operation. The RTD did not explode but was melted, because heat was produced internally faster than it could be transferred out of the heater. It was found that the high

temperature tape was not sufficient to hold the heater RTD in place, but a silicon based adhesive worked well. The other key disadvantage of the RTD was that the time response was very slow, on the order of 10 seconds. The OMEGA[17] catalog was misleading when it claimed a fast response time. The results are demonstrated by two examples. In one example, the heater was run for 10 seconds. The voltage from the sensor was monitored, and it did rise. However, the voltage change was only $\Delta V = 0.000244$. Note that this was with a 3.8mA current. Thus, this corresponded to a resistance change of only 0.0642Ω. The RTD calibration as given by OMEGA[17] reported that there should by a 0.38Ω change for every 1°C = 1.8°F and that it this is linear over a very wide range of temperatures. Thus, it can be inferred that the sensor only detected a 0.31°F change. When the wind was off, that sensor output voltage was constant to 6 decimal places. So the temperature rise was minimal as compared to the wind on case.

Later after the 65v heater was destroyed, another RTD was installed and run at 50v DC. In this case, the heater remained on for 55 seconds. Note that the temperature output was not calibrated to reflect a true temperature since only the ΔT was of importance. The response to this can be seen plotted in Figure 4-3. It should be noted that the "saw tooth" motion of the grid was due to the poor resolution D/A converter.

The curve in Figure 4-3 was used to approximate the RTD sensor time response of 10 seconds. This figure was later confirmed by the OMEGA technical support staff. As can be seen in this figure, it takes almost the full 55 seconds for the temperature to reach near the maximum value. For this case, the sensor output temperature had changed by 2.5°F at 55 sec. However, at 10 sec. into the run there was only about a 0.4°F difference. This was similar to the result for the 65v heater 10 second run, however the due to the poor D/A resolution these results are not precise, but rather show a trend.

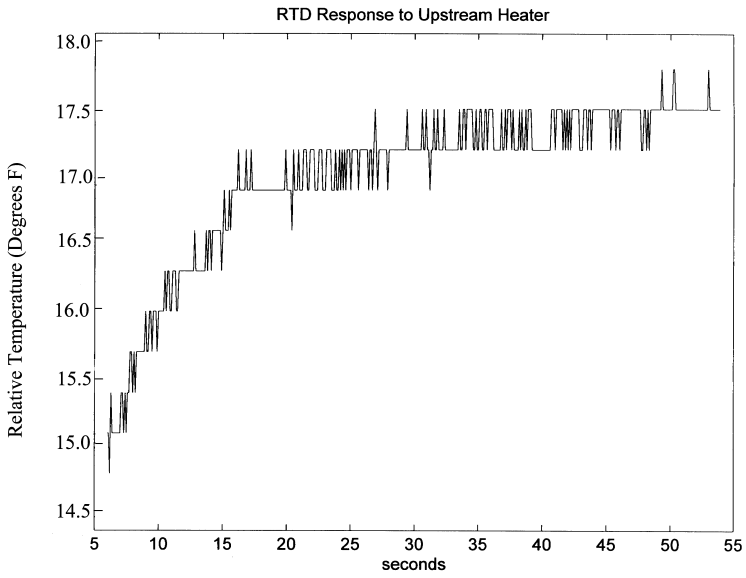

Figure 4-3 Plot of Relative Temperature as measured by a Thin Film RTD for 50v DC RTD heater one inch upstream

While this might be considered a success, the heater was also eventually destroyed at 50v DC. Thus, it was determined that these thin film RTDs make poor heaters when used for steady heat. They also take almost a minute before reaching max. temperature so they are also poor heaters when quick bursts of heat are desired. This is directly related to the other disappointment; the observed time response of the RTD for sensing. If the limiting streamline singularities are to be detected in a timely manner, a sensor response time of this order of magnitude is not acceptable.

Chapter 5 *Analytic Design Study*

The analytic study is essential to the development of the Thermal Grid. This is because it is the tool by which the effects of the various system parameters on the system can be judged as a whole. Since the Thermal Grid works by repeating the same process, it is necessary to only model a single stage in the process. This involves the release of heat from the heater, convection and diffusion downstream, and the response of the sensor. An understanding of each one of these three pieces is essential to understanding the way they work together as a system. The study presented here involves a number of assumptions and idealized representations, but it should prove sufficient as a design tool and as a foundation that later models can build upon.

The governing equation for 3D unsteady heat transfer with convection can be written as.

$$\frac{\partial T}{\partial t}+U\frac{\partial T}{\partial x}+V\frac{\partial T}{\partial y}+W\frac{\partial T}{\partial z}=\frac{\nu_T}{\mathrm{Pr}_T}\left(\frac{\partial^2 T}{\partial x^2}+\frac{\partial^2 T}{\partial y^2}+\frac{\partial^2 T}{\partial z^2}\right) \qquad \textbf{(5-1)}$$

The axis system is defined with the x-coordinate along a streamline, z normal to the wing surface, and y completing the right hand coordinate system. It is assumed that the diffusivity, $\left(\nu_T/\mathrm{Pr}_T\right)$, is constant and equal in all three spatial dimensions. This assumption is made following the steps of the work by Castro and Dianat[22] who solved the above equation, in it's 2-D non-dimensional form, while analyzing pulsed-wire techniques.

Based on boundary layer assumptions, the V and W velocity terms can be considered as negligible as compared to U in the boundary layer. This is expressed in Eq. 5-2.

$$\left[U\frac{\partial T}{\partial x}+V\frac{\partial T}{\partial y}+W\frac{\partial T}{\partial z}\right]_{Streamline}\approx\overline{U}\frac{\partial T}{\partial x} \qquad \textbf{(5-2)}$$

The effective convection velocity along the streamline, $\overline{U}$, will be less than the free stream velocity, U_e, due to boundary layer effects. To more precisely define $\overline{U}$, assume the heated mass is primarily located in the boundary layer log region due to it's proximity to the surface. Taking $\overline{U}$ = $U_{\log\ region}$, past empirical studies[13] show that for turbulent boundary layers, $\overline{U}/u^* = 5.6\,Log_{10}(z^+)+4.9$. Where z^+ is the non-dimensional boundary layer height, $z^+ = z\,u^*/\nu$. Using this, and the definition of u^* as developed for a flat plate turbulent boundary layer, $u^* = 0.17U_e^{0.9}\left(\nu/X_{LE}\right)^{0.1}$ we can solve for $\overline{U}$. From this, it can be seen that, for a fixed z^+, the effective convection velocity is very weakly dependent on X_{LE} which is defined as the distance of a given point from the leading edge. Thus, it is reasonable to consider $\overline{U}$ constant for the small distance between heater and sensor. The turbulent Prandtl number, Pr_T, has historically been considered constant and ν_T can be shown to be constant as well. In the log region of a turbulent boundary layer, we find $\nu_T = 0.41u^* z$, substituting the definition for z^+ we get $\nu_T = 0.41\nu z^+$. It is evaluated at a representative z^+ and is therefore considered constant as well. The fraction ν_T / Pr_T can thus be replaced with a constant $\overline{K}$ for simplification. Additionally, from this point in the derivation, the subscript will refer to the partial differential with respect to the subscribed variable. Making the necessary substitutions into the equation (Eq. 5-1) we arrive at the equation for unsteady temperature, steady 1-D flow along a streamline, and 3-D diffusion as seen in Eq. 5-3.

$$T_t+\overline{U}T_x=\overline{K}\left[T_{xx}+T_{yy}+T_{zz}\right] \qquad \textbf{(5-3)}$$

In finding a solution to this Partial Differential Equation (PDE), it is necessary to define initial and boundary conditions. For simplicity, assume an insulated wall. For the Thermal Grid, the initial condition is the release of heat by the heater. We will consider

this initial heat release to be instantaneous. A real heater would slowly ramp up to it's maximum temperature and then ramp back down to ambient temperature when turned off. This is the time response for a heater. The ramifications of this approximation will be examined in more detail later. The initial condition for an instantaneous burst of heat at time zero is seen in Eq. 5-4. The variable Q is introduced here and is given units of temperature. It is calculated as the temperature a unit volume of air would rise for the amount of heat released, $Q = E/(\rho\, C_P)$.

$$T(0,x,y,z) = Q\delta(x)\,\delta(y)\,\delta(z) \qquad \textbf{(5-4)}$$

The process begins with making use of the Fourier transform in order to transform the PDE into an Ordinary Differential Equation (ODE) which has a known solution. For the transformation to be complete, it is necessary to apply the Fourier Transform in all three spatial dimensions. The three-way Fourier transform, and it's inverse, are defined in Eq. 5-5, a and b respectively.

$$T \equiv (2\pi)^{-3/2} \iiint_{\infty} \hat{T} e^{-i(\omega_x x + \omega_y y + \omega_z z)}\, d\omega_x\, d\omega_y\, d\omega_z \qquad \textbf{(5-5a)}$$

$$\hat{T} \equiv (2\pi)^{-3/2} \iiint_{\infty} T e^{i(\omega_x x + \omega_y y + \omega_z z)}\, dx\, dy\, dz \qquad \textbf{(5-5b)}$$

The hatted variable is thereby defined as the variable transformed into the Fourier domain. Rewriting the equation for 3D heat transfer along a streamline in terms of the transformed variables using Eq. 5-5a; we arrive at Eq. 5-6.

$$(2\pi)^{-3/2} \iiint_{\infty} \left[\hat{T}_t - i\overline{U}\omega_x \hat{T} + \overline{K}\left(\omega_x{}^2 + \omega_y{}^2 + \omega_z{}^2\right)\hat{T}\right] e^{i(\omega_x x + \omega_y y + \omega_z z)}\, dx\, dy\, dz = 0 \qquad \textbf{(5-6)}$$

Taking the integral and remembering that $\overline{U}$ and $\overline{K}$ are constant, we obtain Eq. 5-7.

$$\hat{T}_t - i\overline{U}\omega_x \hat{T} + \overline{K}\left(\omega_x{}^2 + \omega_y{}^2 + \omega_z{}^2\right)\hat{T} = 0 \qquad \textbf{(5-7)}$$

Collecting the temperature terms, one gets the earlier mentioned ODE in Eq. 5-8.

$$\hat{T}_t = \left[i\overline{U}\omega_x - \overline{K}\left(\omega_x{}^2 + \omega_y{}^2 + \omega_z{}^2\right)\right]\hat{T} \qquad \textbf{(5-8)}$$

Likewise, the initial condition in Eq. 5-4 must also be transformed. Doing this, leads to Eq. 5-9.

$$\hat{T}(0,\omega_x,\omega_y,\omega_z) = Q\left(2\pi\right)^{-3/2} \tag{5-9}$$

Solving the ODE in Eq. 5-8 with the given initial condition gives Eq. 5-10.

$$\hat{T} = Q\left(2\pi\right)^{-3/2} e^{\left[i\overline{U}\omega_x - \overline{K}\left(\omega_x+\omega_y+\omega_z\right)\right]t} \tag{5-10}$$

To make physical meaning from the solution, it must be transformed from the Fourier domain back into the spatial domain. Applying the definition of the inverse transform in Eq. 5-5b to Eq. 5-10 yields an equation for T in Eq. 5-11.

$$T = Q(2\pi)^{-3}\iiint_{\infty} e^{\left[i\overline{U}\omega_x - \overline{K}\left(\omega_x+\omega_y+\omega_z\right)\right]t}\, e^{-i\left(\omega_x x+\omega_y y+\omega_z z\right)}\, d\omega_x\, d\omega_y\, d\omega_z \tag{5-11}$$

This simplifies by performing the integration to get Eq. 5-12.

$$T = Q\frac{e^{-\left[\left(x-\overline{U}t\right)^2+y^2+z^2\right]/\left(4\overline{K}t\right)}}{8\left(\overline{K}\pi\ t\right)^{3/2}} \tag{5-12}$$

Thus, we have an analytic solution for the unsteady temperature distribution in spatial coordinates relative to the initial heater. To find the temperature distribution for a point on the surface (z=0), simply insert the x, y coordinates for that point on the surface as well as the appropriate constants. However, because the sensor is not a point, we will consider the average temperature, T_{ave}, over the surface of the sensor. This is found by integrating the temperature distribution and dividing by the area of the sensor while setting z=0. For ease, the temperature sensor is considered to be square with an edge parallel to the streamline. The width of the sensor is noted as 'w'. The variables x_c and y_c are the x and y surface streamline coordinates for the center of the sensor. This integral is shown in Eq. 5-13.

$$T_{ave} = \frac{1}{w^2} \int_{x_c - w/2}^{x_c + w/2} \int_{y_c - w/2}^{y_c + w/2} T \, dy \, dx \qquad \textbf{(5-13)}$$

Substituting and evaluating the integral yields our first significant equation in Eq. 5-14.

$$T_{ave} = -\frac{Q}{8w^2\sqrt{\overline{K}t\pi}} \left\{ \left[erf\left(\frac{\overline{U}t - x_c + w/2}{2\sqrt{\overline{K}t}} \right) - erf\left(\frac{\overline{U}t - x_c - w/2}{2\sqrt{\overline{K}t}} \right) \right] \left[erf\left(\frac{y_c - w/2}{2\sqrt{\overline{K}t}} \right) - erf\left(\frac{y_c + w/2}{2\sqrt{\overline{K}t}} \right) \right] \right\} \qquad \textbf{(5-14)}$$

Matlab was used to examine the behavior of this solution. For a given instant in time, Eq. 5-14 was plotted for a wide range of values for x_c, y_c. The constants were determined by setting $z^+ \approx 54$, which corresponds to the lower edge of the log region. The kinematic viscosity was set to $\nu = 1.5723 \times 10^{-4}$ ft^2/s, as well as $U_e = 200$ ft/s, $Pr_T = 0.7$, $X_{LE} = 2$ ft, and $w = {}^1/_{16}$ in. This flow field should be similar to the wind tunnel case described in Chapter 2 and resulted in constants of $\overline{U} = 114$ ft/s and $\overline{K} = 0.005$. This case will be referred to in this paper as "Case A."

The value of Q is more difficult to set for a real case. This is because of the fact that the heat is released instantaneously in the delta function. To most accurately model a real sensor, we consider a width for the heater, w_h. Then consider the time it would take a small parcel of air to travel over the heater, $t_h = w_h / \overline{U}$. We next consider the amount of heat that the heater would be able to deliver to the fluid per unit time, P. The proper value for P is really the possible heater output multiplied by the efficiency for the transfer of this energy into the air. The heater output is usually a function of the surface area of the heater multiplied by the heater's power density. We will consider a heater with a power density of 20 Watts / in.^{2} as being representative. For w_h = ¼ in. and an 80% efficiency we arrive at P = 5 watts. The amount of energy delivered, E, is then computed, and the temperature to which that amount of heat would raise a cubic foot of air is $Q = P\, t_h / \left(\rho \, C_P \right)$. For this case Q = 4.717x10^{-5}.

A plot of Eq. 5-14 for such as case can be seen in Fig. 5-1. Remember that the heat pulse begins at time zero at x = 0, y = 0. At time t = 0, the spike is a Dirac delta with a volume of Q.

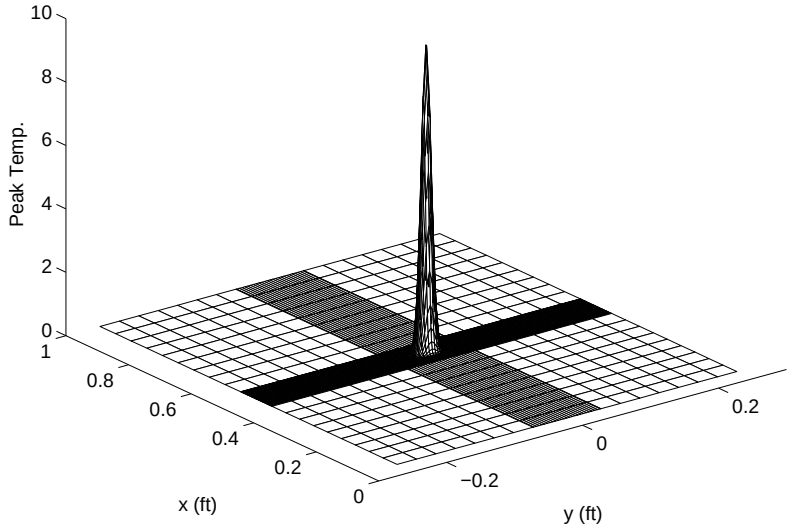

Figure 5-1 Average Sensor Temperature (°F) as a function of Sensor Center position relative to the heater at t=0.057s for Case A

What should be noted from this figure is that for a given instant in time, the temperature distribution is essentially a spike that moves along the x-axis with the effective convection velocity. As it moves downstream, the spike also diffuses in all three spatial dimensions so it essentially gains a larger diameter and lower magnitude. For a fixed location, we can also make a plot of temperature versus time. Such a plot is presented in Fig. 5-2 for $x_c = 0.5$ ft and $y_c = 0$ ft., that is 0.5 ft. downstream of the heater with the streamline passing directly over the sensor. This is what a perfect sensor would observe fixed relative to the heater and streamline. As the heated mass moves over a sensor, the sensor's signal would jump to the peak value such as the case above and then just as rapidly fall back to ambient. The peak value obtained would be recorded. Note that the pulse is only significant for approximately 0.0004 seconds, this is considered the pulse width. Since the initial condition was an instantaneous delta function, the pulse width here is due purely to the diffusion process. This is important because a real heater with width w_h will produce an initial pulse of heat that lasts for t_h seconds. So, the downstream observance of the pulse of heat from a real heater will be wider due to the

addition of the initial width and the diffused width. Since for a ¼ in. heater, $t_h = 1.8x10^{-4}$ seconds, this additional pulse width would increase the pulse width observed here by nearly 50%. While not significant at this point in the analysis, the pulse width is intimately tied to the time response of a real sensor.

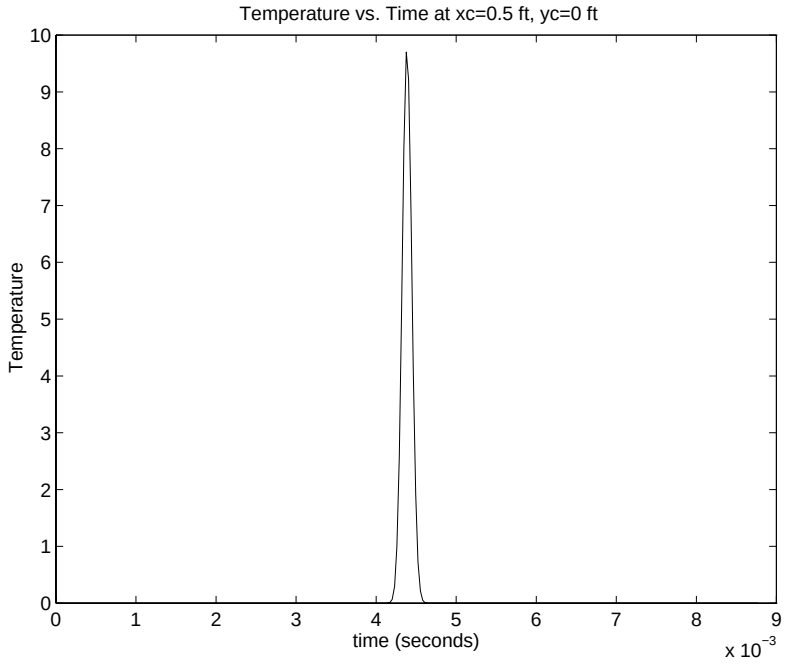

Figure 5-2 Average Sensor Temperature (°F) vs. Time (sec.) for a fixed sensor location for Case A

The peak temperature is valuable information. If the above situation were repeated with an unknown streamline direction, the peak value recorded and the known distance from the heater could be compared against the known peak values for various situations in order to approximately deduce the distance between the sensor and the heated mass path. It is, therefore, necessary to know what this peak temperature would be over the area that surrounds the streamline path.

Using Eq. 5-14, the peak temperature has been determined for the surface $x_c \in [10^{-3}, 1]$ ft. and $y_c \in [0, ¼]$ in. This is presented in Fig. 5-3. Notice that as compared to Fig. 5-1 the scale is compressed to better observe the data. The resulting surface shows, for a given sensor center location, what the maximum observed temperature would be if

that sensor output was plotted like the sensor in Fig. 5-2. This shows that as the heated mass moves downstream it's peak decays rather quickly at first and then slows. It also shows how little lateral diffusion of the heated mass takes place.

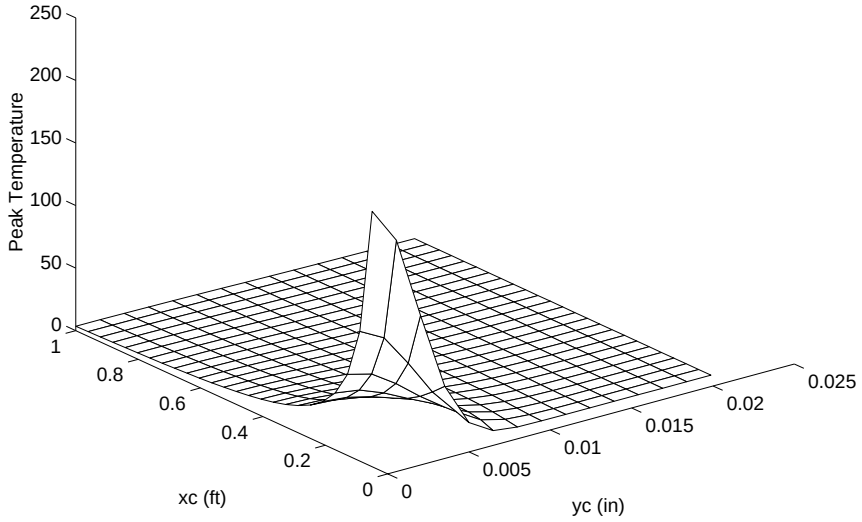

Figure 5-3 Peak Sensor Temperature (°F) as a function of Sensor Center position relative to the heater for Case A

This plot of peak values can also be used to determine the spacing of the sensors. If the sensors are only able to reliably record temperature changes above 1 °F, then the sensors must be spaced such that the worst case heated mass path would register at least that minimum amount at a sensor. The surface plot in Fig. 5-3 is difficult to read, but it gives a good notion as to how the temperature diffuses. An alternate and more accessible means of showing the same information is by generating a contour plot. The contour plot of peak temperatures can be seen in Fig. 5-4. This shows the actual diffusion process even clearer. A given contour of the figure is the perimeter that a sensor must be within to register a temperature at least that of that contour's value. It can be seen that if a slice of the temperature is taken at $y_c = 0.1$ in. then the temperature will initially increase and then fall back down as one moves in the streamline direction. This is because as the heated mass begins it's journey it is very thin and becomes wider through diffusion as it

progresses downstream. As the width increases, the higher temperatures come into the slice. This is the reason for the initial increase. This diffusion process occurs in all three spatial dimensions. The 'x' diffusion adds to the initial pulse width in time, as discussed earlier. The 'z' diffusion represents energy that leaves the surface and is lost. The 'y' diffusion becomes this lateral heated mass width. Eventually, these processes spread the energy to such a degree that the temperature drops off everywhere.

To see how these results would change moving from the wind tunnel to a commercial transport at landing condition, a Boeing 777 is examined. The landing condition is of interest because it is a likely condition when a Thermal Grid might be utilized. The only necessary parameters for this level of analysis are the approach velocity and the chord length, assuming the sensor is located at the trailing edge. The chord will be taken as the chord length just before the kickback. Here U_e = 263.3 ft/s and X = 29 ft. All other factors staying the same, this results in a $\overline{U}$ = 101.42 ft/s and $\overline{K}$ = 0.005. This will be referred to as Case B for the remainder of the paper. The peak temperature contour plot for this condition is located in Fig. 5-5.

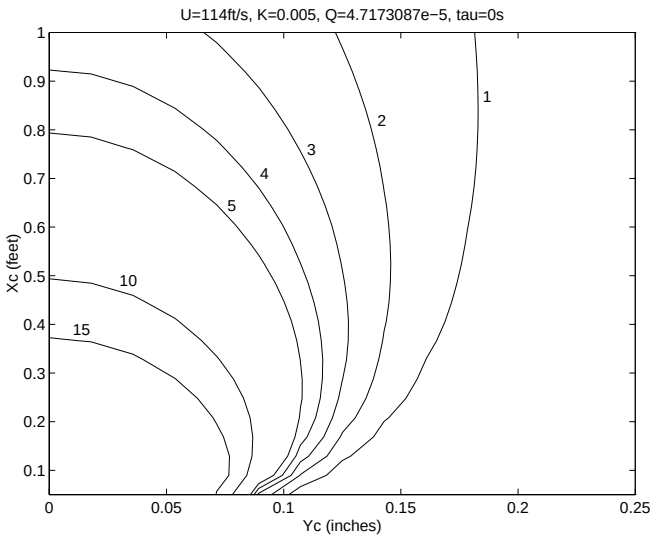

Figure 5-4 Peak Sensor Temperature Contours (°F) as a function of Sensor Center position relative to the heater for Case A

The constant $\overline{K}$, is fixed with respect to the chord and free stream velocity. It will vary with altitude as ν varies. The effective velocity $\overline{U}$ will vary essentially directly with U_e while it varies indirectly with X to the 0.1 power. So, despite the slight increase in U_e the effective velocity drops due to the large chord which gives a thicker boundary layer. The effect of $\overline{U}$ can be seen here. For an 11% reduction in $\overline{U}$ the peak temperatures decay faster along the flow direction (compared to Fig. 5-4). In general, a given contour intersects the streamline axis about 1.5 in. before the wind tunnel case (Case A). This is likely due to the fact that the temperatures decay in time, and it takes longer to move downstream with a lower $\overline{U}$. The unexpected result here is that it does not significantly affect the lateral diffusion, with the contours exhibiting the same lateral dimensions as seen in Fig. 5-4.

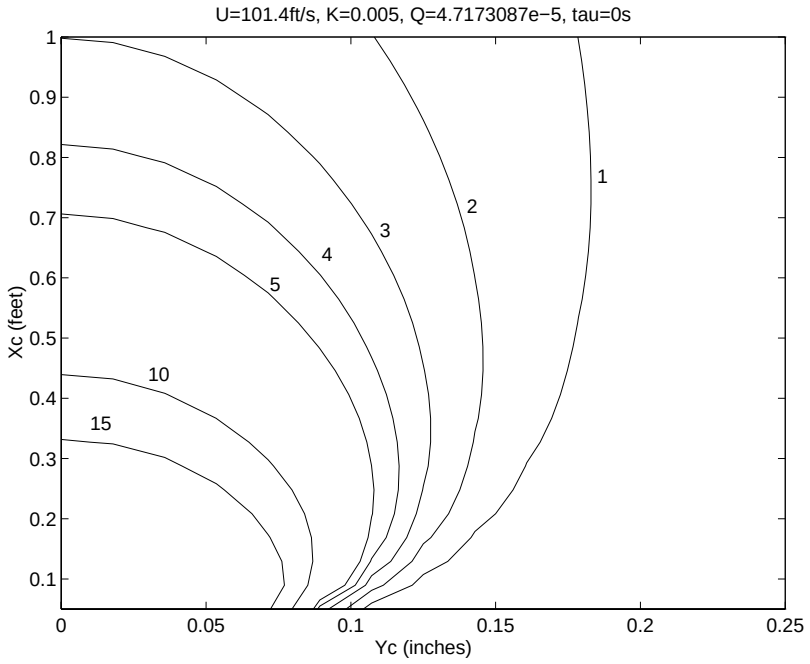

Figure 5-5 Peak Sensor Temperature (°F) as a function of Sensor Center position relative to the heater for a modern transport aircraft at it's landing condition (Case B)

While the data presented so far is useful, it leaves out an important process. In the same way that the heater needs time to ramp up to temperature, the temperature sensor needs time to register a temperature. The time response of the sensor is important,

because, as was seen for a quick burst of heat from the heater, the sensor only sees a slightly diffused instantaneous burst of heat. If the sensor is too slow, it will significantly degrade the temperature reported by the sensor as opposed to the actual surface temperature. The previous cases are therefore limiting cases for a sensor with a zero or perfect time response. For a more precise modeling of the process, we have attempted to incorporate the time response of the sensor. The sensor is modeled to behave according to a linear model as, described by Ogata[18], where θ is the sensor output and the sensor time constant is τ. Thus.

$$\tau \frac{d\theta}{dt} + \theta = T_{ave} \qquad \textbf{(5-15)}$$

Since all temperatures are measured relative to ambient, the ambient temperature is considered to be zero. This gives the initial condition, $\theta(0) = 0$. The solution of Eq. 5-15 can be obtained via Laplace Transforms, where $\Theta(s)$ and $\overline{T}_{ave}(s)$ will denote the Laplace domain representations of θ and T_{ave} respectively. Taking the transform of Eq. 5-15 and rearranging, we get Eq. 5-16.

$$\Theta(s) = \frac{1}{\tau s + 1} \overline{T}_{ave}(s) \qquad \textbf{(5-16)}$$

Using *Mathematica* to transform the sensor input (Eq. 5-14), substituting into the above equation, and then applying the inverse Laplace Transform to Θ gives an equation for the sensor output (Eq. 5-17) for a sensor located at any position on the surface.

$$\theta = \frac{Q}{8\tau w^2 \sqrt{\overline{K}\pi}} \left(-\int_0^t \frac{e^{-t_1/\tau}\, Erf(A_1)\, Erf(C_1)}{\sqrt{t-t_1}} dt_1 + \int_0^t \frac{e^{-t_2/\tau}\, Erf(B_2)\, Erf(C_2)}{\sqrt{t-t_2}} dt_2 + \int_0^t \frac{e^{-t_3/\tau}\, Erf(A_3)\, Erf(D_3)}{\sqrt{t-t_3}} dt_3 - \int_0^t \frac{e^{-t_4/\tau}\, Erf(B_4)\, Erf(D_4)}{\sqrt{t-t_4}} dt_4 \right) \qquad \textbf{(5-17)}$$

where

$$A_n \equiv \frac{\overline{U}(t-t_n)-x_c+w/2}{2\sqrt{\overline{K}(t-t_n)}} \quad n=1,3$$

$$B_n \equiv \frac{\overline{U}(t-t_n)-x_c-w/2}{2\sqrt{\overline{K}(t-t_n)}} \quad n=2,4$$

$$C_n \equiv \frac{y_c-w/2}{2\sqrt{\overline{K}(t-t_n)}} \quad n=1,2$$

$$D_n \equiv \frac{y_c+w/2}{2\sqrt{\overline{K}(t-t_n)}} \quad n=3,4$$

Applying the same constants as used for examining the wind tunnel case (Case A) of Eq. 5-14, we can likewise use *Matlab* to examine the predicted sensor output versus time for the same point as located in Fig. 5-2 (x_c = 0.5 ft, y_c = 0 ft), with a time response of τ = 0.01 seconds. This plot is located in Fig. 5-6.

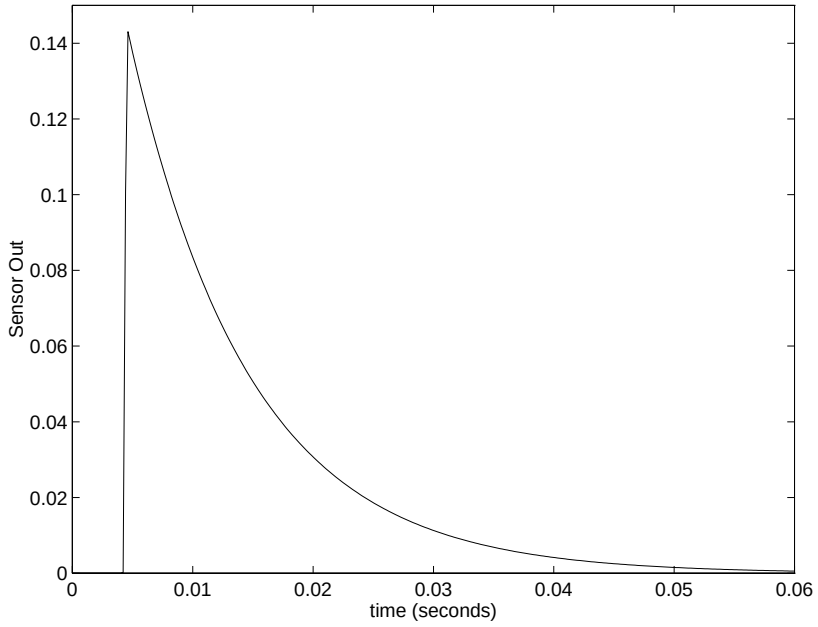

Figure 5-6 Sensor Output (°F) vs. Time (sec.) for a fixed Sensor location with τ = 0.01 seconds for Case A

Although the output rise begins at the same time as in Fig. 5-2, the peak is noticeably reduced in magnitude from 9.7 to 0.14. However, after reaching a maximum it decays much more gradually. In fact, it takes almost 5 ½ time constants to fully cool back to ambient. This is because the time response affects the cool down as well as the process of heating up. The dramatic reduction in the peak occurs because (as could be seen in

Fig. 5-2) the heated mass is over the sensor for only about 0.0004 seconds. Thus, the time response here is 25 times the width of the burst. If the initial heat burst had occurred for a longer period of time, this ratio would be less, and the peak would have been larger. As before, we can also examine contours of the peak sensor output. This has been done for several different time responses, all with the same initial burst of heat. The first of these contours can be seen in Fig. 5-7(a) for a time response of $\tau = 0.1$ sec.

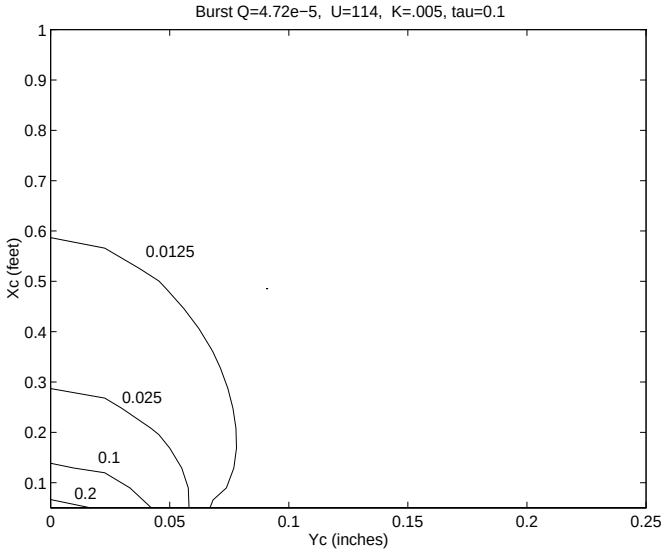

Figure 5-7(a) Peak Sensor Output Contours (°F) for $\tau = 0.1$ sec., as a function of Sensor Center location relative to the heater for wind tunnel conditions (Case A)

The plots for decreasing time responses can be seen in Figs. 5-7(b) , 5-7(c), and 5-7(d) with $\tau = 0.01$ sec. , $\tau = 0.001$ sec., and $\tau = 0.0001$ sec respectively. Examining these contours reveals that for each order of magnitude decrease in the time response, there is a corresponding increase in the peak sensor output of almost an order of magnitude. Only when the time response is less than the width of the heat pulse, do the sensor outputs begin to look similar to the ideal sensor temperature contours in Fig. 5-4. These plots make it clear that the width of the heat pulse as well the time response of the sensor has as much effect on the resulting sensor reading as does the sensor spacing.

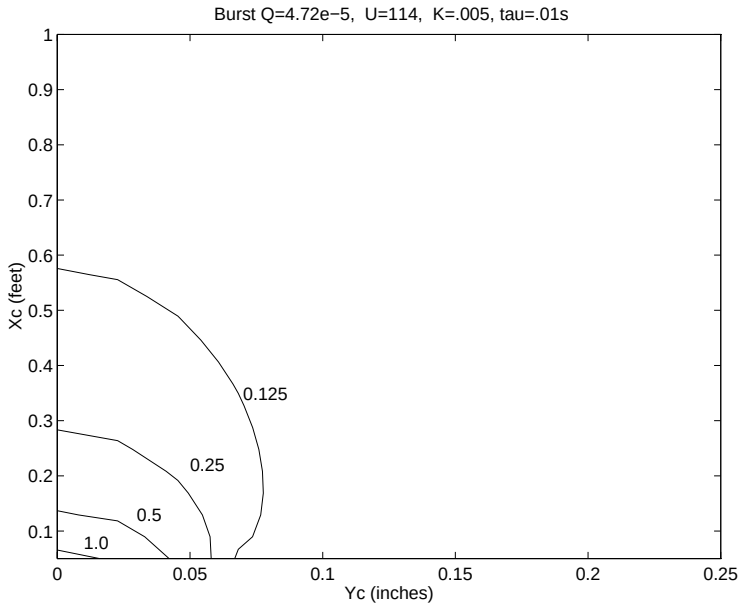

Figure 5-7(b) Peak Sensor Output Contours (°F) for τ = 0.01 sec., as a function of Sensor Center location relative to the heater for wind tunnel conditions (Case A)

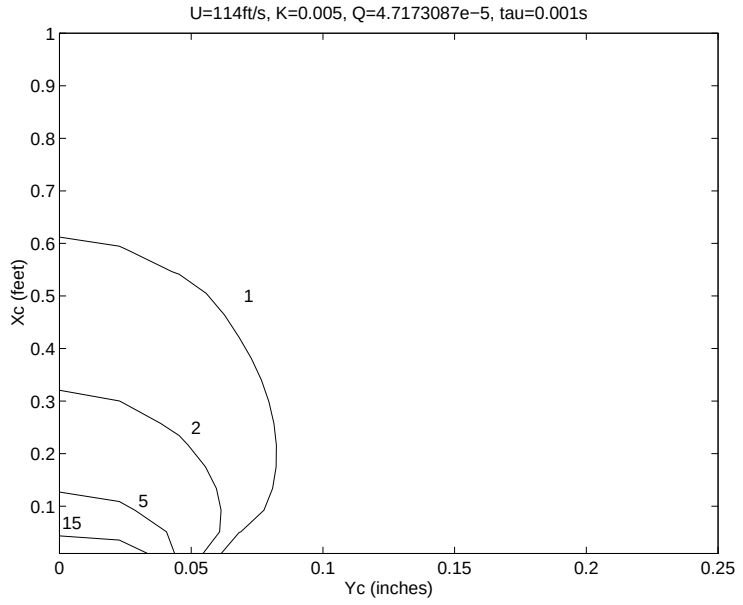

Figure 5-7(c) Peak Sensor Output Contours (°F) for τ = 0.001 sec., as a function of Sensor Center location relative to the heater for wind tunnel conditions (Case A)

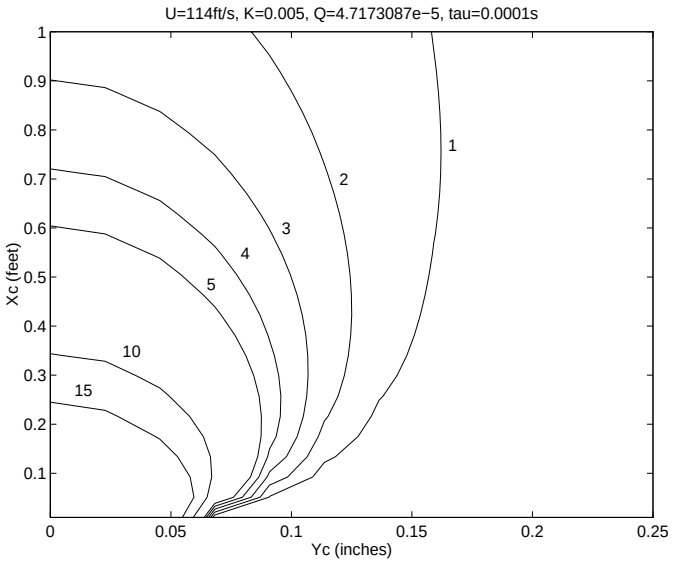

Figure 5-7(d) Peak Sensor Output Contours (°F) for τ = 0.0001 sec., as a function of Sensor Center location relative to the heater for wind tunnel conditions (Case A)

To see the effect of the time response even more clearly, a plot has been made of the peak temperature at a point with decreasing time response. This is seen in Fig. 5-8. The solid line is the true sensor temperature as determined using Eq. 5-14. Notice how the curve is linear until the time response is nearly equal to the width of the heat pulse.

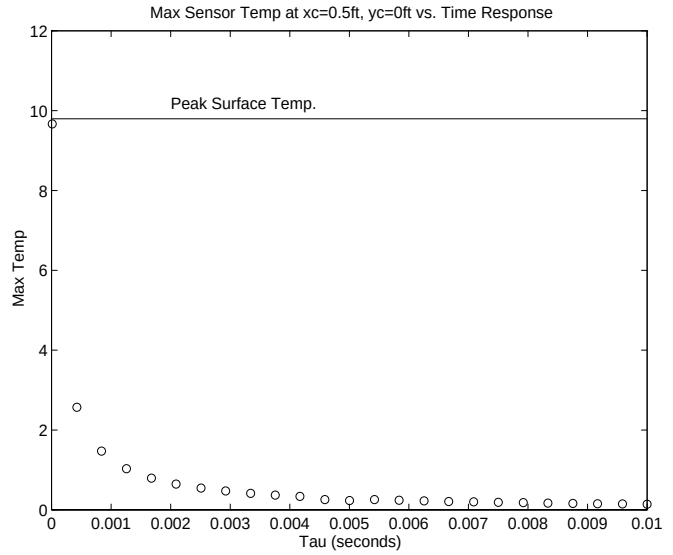

Figure 5-8 Peak Sensor Output vs. Time Response for a fixed Sensor location for Case A

The next step in the modeling is to consider a different heater model. Consider the case where the heater is turned on and stays on. While this is also unlikely, it shows what temperature pattern might be expected when a long heat burst is emitted. To derive an equation for this condition consider Eq. 5-12, then use the principle of superposition to determine the equation for the temperature at time t due to the heat $q\,dt'$ emitted at time t', from time 0 to t. Q is rewritten as q to note the differences. Here, q is based on the amount of energy per unit time as opposed to Q which is based on total energy delivered. Thus, the equation becomes.

$$T = \frac{q}{8\left(\overline{K}\pi\right)^{3/2}} \int_0^t \frac{e^{-\left[\left(x-\overline{U}(t-t')\right)^2+y^2+z^2\right] \Big/ \left(4\overline{K}(t-t')\right)}}{\left(t-t'\right)^{3/2}} dt' \qquad \textbf{(5-18)}$$

Carslaw and Jaeger[19] show the above can be solved by substituting $R^2 = x^2+y^2+z^2$ and then performing a change of variable using Eq. 5-19.

$$\xi = \frac{R}{2\sqrt{\overline{K}\,(t-t')}} \qquad \textbf{(5-19)}$$

Then, manipulate the resulting equation and simplify to yield Eq. 5-20.

$$T = \frac{q}{2\,R\,\overline{K}\,\pi^{3/2}} e^{Ux/2\overline{K}} \int_{R/2\sqrt{\overline{K}t}}^{\infty} e^{-\xi^2-\left(U^2R^2/16\overline{K}^2\xi^2\right)}\, d\xi \qquad \textbf{(5-20)}$$

This equation can be solved when time approaches infinity, $t \to \infty$. For this case the integral can be evaluated as in Eq. 5-21.

$$T = \frac{q}{4\pi\,\overline{K}\,R} e^{-U(R-x)/2\overline{K}} \qquad \textbf{(5-21)}$$

In using Eq. 5-21, we need to determine the constant q. Since q is based on energy per unit time, this is relatively easy. Again, consider a heater capable of transferring 5 watts of energy to the fluid. Thus, to determine q, simply determine the temperature to which 5 joules of energy would raise a cubic foot of air, i.e. q = 0.2581. Lastly, integrate the temperature over the sensor area and divide by the same area to determine an average

temperature over the sensor. Equation 5-21 was integrated using *Matlab* and the peak temperature contours were found at t = ∞. A plot of this is shown in Fig. 5-9.

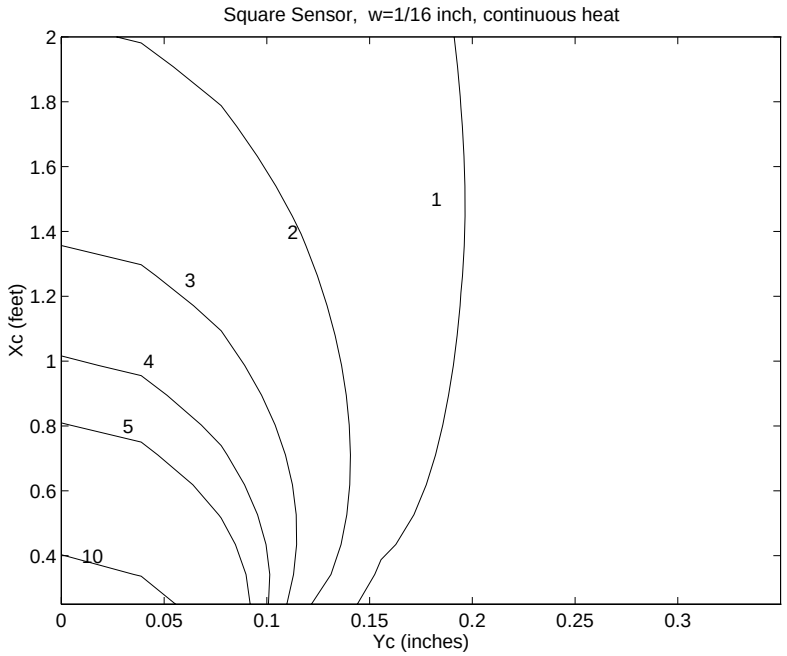

Figure 5-9 Peak Sensor Temperatures (°F) as a function of Sensor Center location relative to the heater at time (t = ∞) for a continuous heater for wind tunnel conditions (Case A)

Since the heat pulse is constant, the time response of the sensor will not be a factor here. This is the primary advantage for a longer heat pulse. However, the time response will still affect the sensor cool-down whenever the heat pulse stops. A close comparison of these contours with those for the peak sensor temperature due to a burst of heat for an otherwise equivalent case, as seen in Fig. 5-6, shows that the peak temperatures for this case are slightly less. This is somewhat of a distortion due to some earlier assumptions. It is important to remember that these are peak temperatures. The case with the instantaneous release of heat compresses all the energy into a very quick burst. Thus, the energy that would have been released over a finite time t_h is released over an infinitely small length of time. Because t_h is very small this is not unreasonable, but the effects are noticeable. When the energy is more compressed, the pulse width will be small and the peak will be lower. The other effect of a long burst of heat is that the lateral diffusion is increased. This is likely due to the fact that the temperatures along the

streamline are constant for a constant heat output. This is as opposed to the previous heater concept where the heat at a given point was fleeting. The net effect of this is to give the temperature at any given point downstream more time in which to diffuse.

With all this information in hand, we can then begin to examine what the constraints on the real system would be. In summary, the effects of the flow field properties, the time response of the heater, as well as the influences of the heat pulse of been observed. Based on this information a baseline design of a Thermal Grid system can be proposed.

Chapter 6 *Preliminary Design of a Thermal Grid*

Considering all that has been learned about the various aspects of the Thermal Grid in the proceeding chapters, a few basic observations can be made that would help bring the idea of the Thermal Grid into better order. One of the primary concerns that was unable to be addressed was how severe the temperature "noise" would be on the wing. The level of this temperature variation as produced by the engine and other sources of heat would determine the necessary signal strength for the Thermal Grid system. For the sake of design 1°F was chosen as a design point for a measurable signal. A study of such temperature variation would better define this term which is integral to the design of a Thermal Grid system.

It was learned from the analytic study that for a heater capable of emitting 5 watts of energy into the flow, a sensor capable of detecting 1°F can be easily located a foot downstream and still detect the heated mass created by the heater. However, during this distance the heat diffuses only slightly laterally. This long, thin thermal trail is difficult to prevent from slipping through the sensor arrangement. However, it is important that the detection be reliable for any in-plane flow so that the flow can be considered out of plane or in a tight spiral if the heat is not detected. This would tend to require a very fine grid resolution, or rectangular shaped heaters that would emit very wide heat patterns. This first choice is expensive, and the second would add a directional bias to the system that is undesirable. There is, however, an alternative. Due to the fact that the heated mass extends so far downstream it is possible to make use of one of the concepts for densely spaced sensors shown in Chapter 3. In this concept, the heated mass is allowed to pass in between the first or perhaps even second row of sensors in the expectation that the following row of sensors might be better situated to capture it. If a square grid node pattern is used, as in the Chapter 3 baseline, the sensors fit this model, see Fig. 3-5.

For our model, a straight line ray is considered to be emitted from a heater, at the axis origin, at an angle of φ off the horizontal. A series of nodal points were then evenly divided in the 1st quadrant of the axis with the distance between nodal points in either dimension being equal and denoted as 'S'. The number of nodal points in each direction was determined by how many times S evenly divided into 1 foot. The minimum distance was determined between the line and the node that was closest to it. This process was repeated for a large number of angles, φ, between 0° and 45°. For this range of angles, the worst case situation was determined, and the distance between this line and it's closest sensor was reported and was noted as 'D'. This distance then determined how wide the thermal path would need to be, for a given spacing, to be detected by a sensor. These distances are shown in Table 6-1.

Table 6-1 Distance from Heated mass center to Sensor center for various Sensor Spacing

'S', (inches) Distance between sensors	'D', (inches) Worst case distance from heated mass to sensor
1	0.0729
2	0.2718
3	0.5716
4	0.9408
5	1.5651
6	1.8781

What this distance 'D' really means in terms of the Thermal Grid development needs to be considered. The contours as seen in the plots in Chapter 5 show the amount of lateral diffusion that occurs to one side of a heated mass. This indicates how far a sensor can be from the edge of the heater and still detect the heated mass, we will note this distance as approximately d_{diff}. The other important aspect is that the heater itself has a finite width, w_h. Thus, for a heated mass to be detected, the center must pass within

$d_{diff} + w_h / 2$ from the center of a sensor. The variable d_{diff} will vary in the stream-wise direction, however for simplicity it is considered as an average constant here. The exact value is a function of all the factors discussed in Chapter 5. These include the length of the heat burst, the time response of the sensor, the sensor size, and the external flow field conditions. However, if the heat burst can be considered to last approximately 4-5 time constants, then perfect sensor conditions could be considered. The trade-off is that the sensor must be allowed the same 4-5 time constants to return to ambient temperature. For a time constant of around than 0.1 seconds this seems reasonable.

The OMEGA catalog[17] is considered to be a good indicator of what is available in terms of mainstream 1996 technology. This shows that it is possible to get a time response of 0.1 seconds, in moving air, with a thermocouple made of butt-welded 0.004 in. diameter wire. It is possible to achieve a time response as low as 0.003 sec. for a butt-welded wire diameter of 0.001 in. However, this would seem to be excessively fragile. Beaded-type thermocouples are also possible, but are generally about 50% slower. The thin film RTDs used in Chapter 4 have a much larger time constant of about 15 seconds. This value was inferred from the experiments in Chapter 4. In order to make use of such a slow sensor, a very hot heater could be utilized and consider that only a partial response is necessary from the sensor. It was also determined in Chapter 4 that the RTDs make generally poor heaters. This could be studied in more detail, but without a single device capable of acting as both a heater and sensor, a thermocouple is preferable. There are other sensor possibilities as well. These would include heat transfer sensors, and thermistors, as well as hot-films and hot-wires. While some of these might achieve even better time responses, they are also much more expensive.

For an example, consider a reasonable time constant ($\tau = 0.1$ seconds) with a heat burst about 0.5 seconds long. Because the burst is much larger than the time response, we can consider the contour for a perfect sensor as seen in Fig. 5-4. For very long heater runs, an additional amount of diffusion can be expected as seen in Fig. 5-13. However we will attempt to be conservative. From this, $d_{diff} \approx 0.15$ in. can be seen for the 1°F contour.

Add this to $w_h / 2$ for the ¼ in. heater as used in Chapter 5 and it can be seen that we need a $D < 0.275$. Table 6-1 can now be used to show that the sensor spacing needs to be 2 inches. This spacing could be increased for a larger heater, or for a more sensitive sensor, or even a different sized temperature sensor, but the trends and methods are clear.

The argument above is presented so that a heated mass will not escape detection without an unlikely contorted path. Yet there are other arguments that still need to be made. It should be obvious that the spacing of the sensors is directly related to the number of sensors required to cover a given area. This is turn is directly related to cost, as well as to maintenance. However, a densely spaced arrangement carries with it the arguments as presented in Chapter 3 for reliability. This needs to be weighed against desired performance levels that can not be determined at this time.

The other key point is that the purpose of this system is to detect singularities in the limiting streamlines. It should be remembered from the Introduction that one of the primary forms of these singularities is an in-plane spiral. Such spirals or vortices were seen in the oil flows shown in Chapter 2 from the stability tunnel tests and in the literature. The stability tunnel tests further showed that, for our wing model, these were some of the first signs of separation at the trailing edge, and that initially they are fairly small. If complete confidence is to be had in the system, then the sensor spacing should be fine enough to capture these spirals in the flow. The 2 in. sensor spacing proposed in the example should be sufficient, with the heaters spaced at least every foot.

It should also be noted that those familiar with thermal tufts will recognize the Peclet number. This number was found to need to be at least 50 for proper sensitivity by Bradbury and Castro[20]. For numbers greater than this a sensor will always detect the convected portion of the heat before any conducted heat. This is not a problem for the relatively large distances here. For the stability tunnel case, and with the definition of the Peclet number in Eq. 6-1, the distance between heater and sensor must be at least 1/16 in. apart to satisfy this criteria.

$$Pe = \frac{S V}{\bar{\bar{K}}} \qquad \textbf{(6-1)}$$

This study thus demonstrates that it is possible to construct a working Thermal Grid. A thermocouple such as that described in this chapter can be easily purchased. It should also be remembered that a system will be placed on a wing with prior knowledge as the where on the wing separation is likely to be expected. Keeping the sensors in this focused region and using the off-the-shelf components. This should serve as a first step for any future designs or wind tunnel investigations.

Chapter 7 *Conclusion*

All this shows quite clearly that the Thermal Grid is a viable, cost effective, and rugged means of detecting 3D flow separation on a finite wing. It is also clear that this work has just begun to scratch the surface of all the details that need to be investigated before a final system could ever be flight tested. One of the primary questions that still needs to be answered is the time scale such a system would be able to work within. This is difficult because so little is know about the development of separation. It is also difficult to determine a required signal level without knowing the temperature noise that would be present on a wing. Other questions remain in terms of a more detailed analytical model and the logic behind such a system. The logic would need to determine when to trigger which heaters, while keeping track of multiple heated masses at any given instant. It will also need to take this information and make decisions about the resulting patterns that might infer separation. In conclusion, there is still necessary work ahead for the proper development of the Thermal Grid. In conclusion:

1. 3-D surface flow separation can be predicted by tracing surface streamlines.
2. The Thermal Grid has been proposed and shows potential for tracing surface streamlines so that separation can be inferred.
3. A preliminary Thermal Grid design has been proposed that makes use of only current off-the-shelf technology.

4 There is much work that remains to be done on improving the detail of the analytic model, and for future wind tunnel verification.

References

1. Smith, A.M.O. (1975), "Remarks on Fluid Mechanics of the Stall," AGARD-LS-74, Aircraft Buffeting and Stalling.
2. Lynch, F.T. (1982), "Commercial Transports - Aerodynamic Design for Cruise Performance Efficiency," Transonic Aerodynamics, ed. Nixon, D. Progress in Astronautics and Aeronautics, Vol. 81, AIAA New York
3. Shevell, R.S. and Schaufele, R.D. (1966), "Aerodynamics Design Features of the DC-9," Journal of Aircraft, Vol. 3, No. 6, pp. 515-523
4. Wagenamakers, J. (1991), Aircraft Performance Engineering, Prentice Hall
5. Cooke, J.C. and Brebner, C.G. (1961), "The Nature of Separation and it's Prevention by Geometric Design in a wholly Subsonic Flow," Lachman, G.V., Boundary Layer and Flow Control, it's principles and application, New York, Pergamon Press
6. Prandtl, L. (1905), "Grenzschichten und Widerstand," Verhandlungen des III, Internationalen Mathematiker-Kongresses, Heidelberg, 1904
7. Simpson, Roger L. (1985), "Two Dimensional Turbulent Separated Flow," AGARD-AG-287-Vol. 1.
8. Marshakov, A.V. and Schetz, J.A. (1994), "Direct Measurements of Skin Friction in a Turbine Cascade," 30th AIAA/ASME/SAE/ASEE Joint Propulsion Conference, AIAA 94-3076
9. Eaton, J.K., Jeans, A.H., Ashjaee, J., and Johnston, J.P. (1979), "A Wall Flow-Direction Probe for use in Separating and Reattaching Flows," J. Fluids Engineering, 101, pp 364-366
10. Eaton, J.K., Westphal, R.V., and Johnston, J.P. (1982), "Two New Instruments for Flow Direction and Skin Friction Measurements in Separated Flows," ISA Trans., 21 pp 69-78
11. Shivaprasad, B.G. and Simpson, R.L. (1982), "Evaluation of an Improved Wall-Flow-Direction Probe for Measurements in Separated Flows," J. Fluids Engineering, TSAME, 104, pp162-166

12. Fletcher, J.C., Mateer, G.C., and Brosh, A. (1977) US Patent No. 4,061,029
13. Schetz, J.A. (1993), Boundary Layer Analysis, Prentice Hall, Englewood Cliffs, New Jersy
14. Wang, K.C. (1976), "Separation of Three Dimensional Flow," Proceedings of the Lockheed-Georgia Company Viscous Flow Symposium, June 22-23, 1976
15. Vanino, R. and Wedemeyer, E. (1971), "Wind Tunnel Investigation of Buffet Loads of Four Airplane Models," AGARD-CP-84-71
16. Tobak, M. and Peake, D.J. (1982), "Topology of Three-Dimensional Separated Flows," Annual Review of Fluid Mechanics, Vol. 14, pp. 61-85
17. OMEGA, (1992), Complete Temperature Measurement Handbook and Encyclopedia, Vol. 28
18. Ogata, K. (1992), System Dynamics, Prentice-Hall Inc.
19. Carslaw, H.S. and Jaeger J.C. (1959), Conduction of Heat in Solids, Oxford Press
20. Bradbury, L.J.S. and Castro I.P. (1971), "A Pulsed-Wire Technique for Velocity Measurement in Highly Turbulent Flow," J. Fluid Mechanics, Vol 49, pp 657-694
21. Yates, L.A. and Chapman, G.T. (1992) "Streamlines, vorticity lines, and vorticies around three-dimensional bodies", AIAA J. 30, 1819-1826
22. Castro, I.P. and Dianat, M. (1990) "Pulsed-Wire Velocity Anemometry Near Walls", Experiments in Fluids, Vol. 8, pp. 343-352

Appendix A *Matlab Codes*

Matlab Code used to determine Peak Average Sensor Temperature over Wing Surface for a pulse heater

```
w = 1/(16*12);
mxtmp = [];
temp = [];
Q = 4.7173087E-5;
Nt = 25;
NX = 25;
NY = 15;
y1 = linspace(0,0.25/12,NY);
x1 = linspace(0.05,1,NX);
kbar = 0.005;
U = 101.42;
for j = 1:NX
   for k = 1:NY
      xc = x1(j);
      yc = y1(k);
      result = -0.1;
      t = xc/(U+0.5);
      i = 0;
      while i < Nt
         A = 8*w^2*sqrt(kbar*t*pi);
         B = erf((U*t-xc+w/2)./(2*sqrt(kbar*t)));
         C = erf((U*t-xc-w/2)./(2*sqrt(kbar*t)));
         D = erf((yc-w/2)./(2*sqrt(kbar*t)));
         E = erf((yc+w/2)./(2*sqrt(kbar*t)));
         a = -Q./A.*(B-C).*(D-E);
         if a >= result
            result = a;
            t = t + 0.000005;
            i = i+1;
         else
            i = Nt;
         end
      end
      if result == -.1
      disp('BAD pt.')
      end
      temp = [temp, result];
   end
   mxtmp = [mxtmp;temp];
   temp = [];
```

Matlab Code used to determine Peak Sensor Output over Wing Surface for a pulse heater

```
global tau time
wx = 1/(16*12);
wy = wx;
mxtmp = [];
temp = [];
tau = 0.01;
Q = 4.7173087E-5;
Nt = 28;
NX = 25;
NY = 12;
y1 = linspace(0,0.25/12,NY);
x1 = linspace(0.01,1,NX);
for j = 1:NX
   for k = 1:NY
      xc = x1(j)
      yc = y1(k)
      result = 0;
      time = xc / 115;
      i = 0;
      while i < Nt
         a = Q * sensor(xc,yc,wx,wy)
         if a >= result
            result = a;
            time = time + 0.000005;
            i = i+1
         else
            i = Nt
         end
      end
      temp = [temp, result];
   end
   mxtmp = [mxtmp;temp];
   temp = [];
end
```

Matlab Code as used to determine Average Sensor Temperature at a fixed location over a range of Time for a pulse heater

```
w = 1/(16*12);
Q = 4.7173087E-5;
yc = 0;
xc = 0.5;
kbar = 0.005;
U = 114;
Nt = 300;
t1 = linspace(1e-5,8.772e-3,Nt);
temp = [];
for i = 1:Nt
  t = t1(i)
  A = 8*w^2*sqrt(kbar*t*pi);
  B = erf((U*t-xc+w/2)./(2*sqrt(kbar*t)));
  C = erf((U*t-xc-w/2)./(2*sqrt(kbar*t)));
  D = erf((yc-w/2)./(2*sqrt(kbar*t)));
  E = erf((yc+w/2)./(2*sqrt(kbar*t)));
  a = -Q./A.*(B-C).*(D-E);
  temp = [temp,a];
end
```

Matlab Code to determine Sensor Output for a fixed sensor location over range of Time for a pulse heater

```
global tau time
wx = 1/(16*12);
wy = wx;
tau = 0.01;
Q = 4.7173087e-5;
Nt = 300;
yc = 0.0;
xc = 0.5;
t1 = linspace(1e-6,6e-2,Nt);
temp = [];
for i = 1:Nt
   time = t1(i);
   a = Q * sensor(xc,yc,wx,wy);
   temp = [temp, a];
end
```

Matlab Code as used to determine Average Sensor Temperature over Wing Surface at an Instant in time for a pulse heater

```
w = 1/(16*12);
tmp = [];
temp = [];
Q = 4.7173087E-5;
Nx1 = 10;
Ny1 = 8;
Nx2 = 50;
Ny2 = 25;
x2 = linspace(0.05,0.45,Nx1);
y2 = linspace(-0.25,-0.05,Ny1);
x3 = linspace(0.451,0.549,Nx2);
y3 = linspace(-0.049,0.049,Ny2);
x4 = linspace(0.55,1,Nx1);
y4 = linspace(0.05,0.25,Ny1);
x1 = [x2,x3,x4];
y1 = [y2,y3,y4];
kbar = 0.005;
U = 114;
t = 0.5/114
for j = 1:length(x1),
   xc = x1(j)
   for k = 1:length(y1),
      yc = y1(k);
      A = 8*w^2*sqrt(kbar*t*pi);
      B = erf((U*t-xc+w/2)./(2*sqrt(kbar*t)));
      C = erf((U*t-xc-w/2)./(2*sqrt(kbar*t)));
      D = erf((yc-w/2)./(2*sqrt(kbar*t)));
      E = erf((yc+w/2)./(2*sqrt(kbar*t)));
      a = -Q./A.*(B-C).*(D-E);
      temp = [temp, a];
   end
   tmp = [tmp;temp];
   temp = [];
end
```

Matlab Code to determine the Peak Sensor Output for a fixed sensor location for a range of time responses for a pulse heater.

```
global tau time
wx = 1/(16*12);
wy = wx;
temp = [];
Q = 4.7173087E-5;
Nt = 28;
Ntau = 25;
yc = 0;
xc = 0.5;
tauspan = linspace(0.00001,0.01,Ntau);
for j = 1:Ntau
   tau = tauspan(j)
   result = -0.5;
   time = xc / 114.2;
   i = 0;
   while i < Nt
      a = Q * sensor(xc,yc,wx,wy)
      if a >= result
         result = a;
         time = time + 0.000005;
         i = i+1;
      else
         i = Nt;
      end
   end
   temp = [temp, result];
end
```

Matlab function 'Sensor' which determines the Average Sensor Output for a fixed location at a fixed instant in time for a pulse heater.

This function is called by all other routines which determine the sensor output in one form or another.

```
function [Out] = sensor(xc,yc,wx,wy)

global time Kbar Ubar x1 y1 tau

Ubar = 114;
Kbar = 0.005;
tol = 1e-4;
endtime = time - 1e-9;
constant = -1/(8*sqrt(pi)*wx*wy*sqrt(Kbar)*tau);

x1 = xc - wx/2;
y1= yc - wy/2;
int1 = quad8('subexp1',0,endtime,tol);
x1 = xc + wx/2;
int2 = quad8('subexp1',0,endtime,tol);
y1 = yc + wy/2;
int4 = quad8('subexp1',0,endtime,tol);
x1 = xc - wx/2;
int3 = quad8('subexp1',0,endtime,tol);
Out = constant*(int1 - int2 - int3 + int4);
```

Matlab function which determines the integrand as used in the function Sensor

```
function [out] = subexp1(x)

global time Kbar Ubar x1 y1 tau

c = (time - x)*Ubar - x1;
e = c./(2*sqrt(Kbar*(time-x)));
f = y1./(2*sqrt(Kbar*(time-x)));
a = exp(-x/tau).*erf(e).*erf(f);
b = sqrt(time - x);
out = a./b;
```

Matlab Code to determine the Average Sensor Temperature over the Wing Surface at time Infinity for a heater that remains on.

```
temp = [];
Q = (0.0516262261)*5.;
NX = 20;
NY = 10;
y1 = linspace(0,0.25/12,NY);
x1 = linspace(0.25,1,NX);
for j = 1:NX
   for k = 1:NY
      xc = x1(j);
      yc = y1(k);
      result = heat(xc,yc,Q);
      temp = [temp, result];
   end
   tmp = [tmp;temp];
   temp = [];
end
```

Matlab function Heat as called from previous Matlab Code to determine the Average Sensor Temperature over the Wing Surface at time Infinity for a heater that remains on.

```
function [out] = heat(xc,yc,Q)

global K U Q

wx = 1/(16*12);
wy = wx;
U = 114;
K = 0.005;
tol = 1e-5;
x1 = xc - wx/2;
x2 = xc + wx/2;
y1 = yc - wy/2;
y2 = yc + wy/2;
temp = quad2dg('heaton',x1,x2,y1,y2,tol);
out = temp/(wx*wy)
```

Computes the integrand for the function Heat.

```
function [out] = heaton(x,y)

global Q K U

A = exp((U*(-x + sqrt(x.^2 + y.^2)))/(2*K));
B = sqrt(x.^2 + y.^2);
```

```
out = Q./(4*K*pi*A.*B);
```

2D Integration routine as used in the case for the constant heater

The 2D integration was performed using a Matlab toolbox written by Howard Wilson and Bryce Gardner. The original routines were obtained from NETLIB. Specific routines used employed a Gauss-Chebyshev method to perform the integration. These routines were obtained via the Internet at www.mathworks.com in the User Written M-Files Section.

Vita

Norman Wesley Gimbert II

I have lived most of my life in the state of Virginia. Growing up in Norfolk, and later attending high school in Fairfax county. After graduating high school in 1990, I attended Va. Tech where I received my Bachelors degree in Aerospace Engineering. During my time at Va. Tech several key events happened in my life. During what would have been my Junior year, I took the opportunity to travel to Zhukovsky, Russia where I was an exchange student for a year at the flight division of the Moscow Institute of Physics and Technology. It was this that taught me, more than anything else, how we take so much for granted. The second significant event was when I first started dating Kim. Kim and I were married in July of 1996. It has been her understanding of me, that many times has helped me understand myself.

After completing the work for my Masters, my wife and I will make the move to Cincinnati OH. There I will begin work for GE aerospace engines as a member of their technical leadership program.